Multiphysics Simulation of a Microwave Atom Chip

A thesis presented in Candidacy for Departmental Honors in Physics

from

The College of William and Mary in Virginia

By

Ksenia (Kisa) Avrutina

April 29, 2026

Accepted for Honors

Seth Aubin

Advisor: Prof. Seth Aubin

Ran Yang

Prof. Ran Yang

Hannes Schniepp

Prof. Hannes Schniepp

Acknowledgements

I would like to thank my faculty mentor, Professor Seth Aubin, for his continued support throughout both this research and my time at William & Mary. I would also like to thank the members of the Ultracold AMO laboratory, both current and past, for their guidance and resources. In particular, I thank William Miyahira for contributing much of the foundational research relevant to this project and Trevor Tingle for his support within the lab. I thank Emmanuel Sampson, my capstone project partner, for his encouragement and assistance throughout this year and all the work he has put into the mechanical device needed for future steps of this research. Additionally, I would like to thank Professors Ran Yang and Hannes Schniepp for being part of my thesis committee. Finally, thank you to my friends and family who have always encouraged me to be the best version of my self, both as a student and researcher.

Contents

List of Figures

Abstract

Microwave atom chips are instrumental in atom interferometry, a technique enabling inertial navigation measurements, ultra-precise gravimetry, and the development of novel quantum technologies. The atom chip uses the near field minima and gradients generated from a microwave transmission line on a dielectric substrate to trap and manipulate ultracold atoms. In order for this device to be implemented to its full potential, it is necessary to create a robust computational model that can be used to simulate various design variations, driving modes, phase differences, and excitation frequencies. This research presents a series of models and the electromagnetic and thermal simulations used to achieve solutions that can be used predict field and current minima, even vs odd mode behavior, wave interferences, and thermal impacts. The models consist of single trace, two-trace, and long two-trace microstrip designs. The last model presented attempts to generate a microwave lattice using two long parallel microwave transmission lines.

Chapter 1

Introduction

1.1 Motivation

Microwave circuits serve as groundbreaking solutions in electromagnetics, communication systems, and quantum sensing. In the realm of quantum sensing, microwave circuits can be used to trap and manipulate atoms along a microwave trace [1]. This technique is known as atom interferometry. Atom interferometry can be used to measure phase shifts in atomic matter waves (as defined by the de Broglie wavelength), in such a way that any changes in local fields and forces are converted into detectable signals. This is essential to inertial navigation systems, as it enables precise acceleration measurements. From acceleration, the position, orientation, and velocity can be determined with no external signals. Similarly, local gravitational acceleration can be measured using atom interferometry. These measurements facilitate underground mapping and provide valuable insights into the geophysical structure and elemental composition of the earth below, as well as on other planets.

This atom trapping can be achieved using two parallel microwave traces on a chip, called here the "microwave atom chip" [1]. When microwave signal propagates through parallel

microwave traces, magnetic near field distributions are generated. The spatial configuration of this magnetic field is dependent on the geometry of the chip, the direction of current through the traces, and the phase difference between the microwave frequencies on either trace. Given appropriate conditions, a magnetic field minimum can be generated in the trapping region between traces. These minima can confine atoms for interferometry. This behavior has been studied for both two-microstrip and three-microstrip (Fig. 1.1) geometries [1]. When atoms are suspended microns above the surface of the chip, they can act as probes for short-range forces and near-fields. Multiphysics simulations can be used to predict the distribution of relevant electromagnetic fields and evaluate the effects of coupling between microstrips and excessive heating on chip performance.

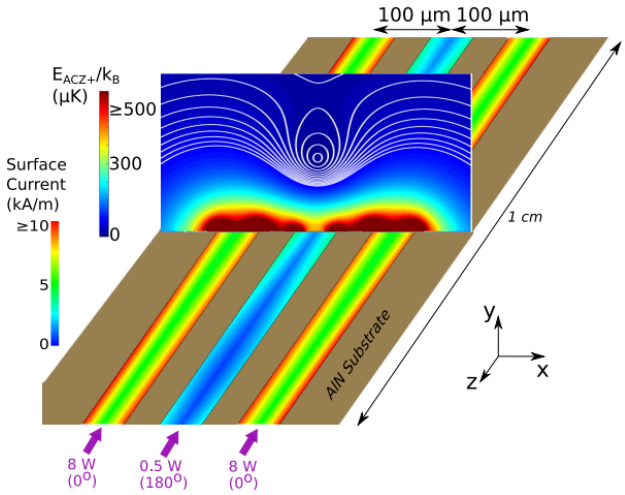

Figure 1.1: Simulation of the three-microstrip model with 6.8 GHz inputs [1].

1.2 Problem Statement

The microwave atom chip's performance is highly dependent on the electromagnetic near-fields, microstrip geometries, and material properties of the chip. Developing a robust simulation model to evaluate how differences in phase, frequency, excitation, geometry, and thermal effects influence electromagnetic and current distributions is essential for the design

and optimization of microwave atom chips, where performance is governed by the efficacy of near-field manipulation and trapping. This work focuses on the two-microstrip model, as opposed to the three-microstrip model, as the underlying physics of this model are more readily interpretable. This makes the two-microstrip model better suited for the varying of multiple variables.

1.3 Project Objectives

The objectives of this research are to:

1. Design and build a microwave atom chip model in Ansys HFSS.
2. Run electromagnetic simulations to verify that the model demonstrates intended behavior.
3. Run thermal simulations to measure expected heating on the chip.
4. Adjust the model geometry to optimize chip performance and study behavior-of-interest.
5. Compare electromagnetic response of traces under various modes of excitation.
    - Single-trace excitation.
    - Dual-trace excitation with varied phase differences.
6. Demonstrate a microwave lattice.

1.4 Scope and Constraints

This project evaluates magnetic field, surface currents, and temperature on a microwave atom chip. These variables are evaluated for both a chip with a single 4.2 mm long trace and two parallel 4.2 mm long traces. These simulations are run for both single trace and dual trace excitation. For dual trace excitation, solutions are found for both even mode (in-phase current, phase difference of $\phi = 0°$) and odd mode (out-of-phase current, phase difference of $\phi = 180°$). Other "in-between" phase variations, $\phi = 90°$ and $\phi = 270°$, are not solved for. Frequencies of 6.8 GHz and 15 GHz are solved for.

In the case of the large scale model with two parallel 24 mm long traces, only magnetic field and surface currents for single phase excitation. As this model is a lot larger and more intensive to run, dual trace excitation, phase variations and thermal solutions were not solved for. As higher frequency behaviors are of interest for this model, frequencies of 15 GHz and 30 GHz are solved for.

1.5 Microwave Atom Chip Assembly System

An assembly system for such a microwave atom chip was developed and is detailed in a separate report written by Ksenia Avrutina and Emmanuel Sampson. This assembly system operates on a larger prototype of the microwave atom chip and enables the manipulation and attachment of additional components onto the atom chip. The additional component attached onto the atom chip is a tapered copper-and-dielectric wedge placed at the inputs of the planar circuit. This tapered wedge ensures gradual changes in geometric dimensions between the narrow copper trace and the wider coaxial cable input. Abrupt changes in trace or substrate dimensions introduce impedance and electromagnetic mode discontinuities, pro-

ducing unwanted reflections and degrading transmission performance. The wedge prevents these unwanted effects, which allows for high power and varied-phase inputs to the atom chip, which are explored in this thesis.

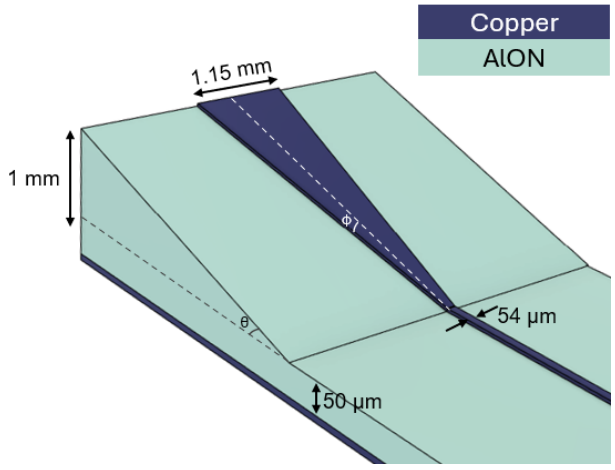

Figure 1.2: Tapered wedge and trace aligned with microwave transmission line.

1.6 Thesis Organization

This introductory chapter provided an overview of the project's motivation, objectives, and scope. The following section, Chapter 2, will provide theoretical background on the physics governing the microwave atom chip, an overview on previous research, and an explanation of the assumptions and approximations made in the Ansys HFSS model. Chapter 3 will further detail the model used in the simulation, solution convergence verification, and data acquisition. Chapter 4 will proceed to discuss the results of these simulations and observations made. Chapter 5 will compare these simulations to theory and discuss potential sources of error and limitations of the model. Chapter 6 will conclude this report with an evaluation of whether this research met its objectives, how it serves the broader motivation, and where it could go in the future.

Chapter 2

Theoretical Background

2.1 Literature Review

The device studied in this work, the microwave atom chip, consists of two parallel microstrips on a dielectric substrate. The microwave near-fields generated by the signal inputs of the microstrips are used for atom interferometry. In their comprehensive review of the subject, Cronin et al. describe atom interferometry as the coherent manipulation of the translational motion of atoms, combined with the scientific applications of this manipulation [2]. The device presented in this thesis is intended for the trapping of ultracold atoms, which are laser-cooled to near-zero (in the range of μK or nK). Ultracold atoms can be slowed to a near-motionless state, enabling their use in atomic clocks, quantum sensors, and other quantum technologies.

Laser cooling and trapping of atoms has been a subject of great interest and study since the 80s. In 1997, the Nobel Prize in physics was awarded jointly to Steven Chu, Claude Cohen-Tannoudji, and William D. Phillips for their work in the field of laser cooling and atom trapping. W. Phillips and H. Metcalf were among the first to demonstrate laser-cooled

deceleration of neutral atoms in 1981 [3]. In prior years, successful laser-cooling attempts were mainly restricted to positive ions, as demonstrated by W. Neuhauser, M. Hohenstatt, P. Toschek, and H. Dehmelt in 1978 [4]. To maintain atom resonance during the cooling process, Phillips and Metcalf applied a spatially varying magnetic field to provide a changing Zeeman shift. As the atoms decelerated, their frequencies shifted due to Doppler shift. By exploiting the Zeeman shift, Phillips and Metcalf were able to compensate for this change in frequency and keep their atoms in resonance. This research laid the groundwork for modern laser cooling techniques, which use the same Zeeman slowing and magneto-optical trapping principles to create ultracold atoms.

A major application of laser-cooling and atom trapping is in the formation of Bose-Einstein condensates (BECs). BECs are a unique state of matter formed when a gas of bosons at low density is cooled to temperatures close to 0 K. At this extremely low temperature, the de Broglie wavelengths $\lambda = \frac{h}{mv}$ of the individual atoms begin to overlap, and so a large fraction of bosons collapse to the ground state. Then, when the bosons occupy the same state, they begin to behave like a single large atom. The group of atoms can then be described by a single macroscopic wavefunction, allowing quantum mechanical effects to be visible to the human eye. The BEC was first predicted by Einstein, and was first created in 1995 by Eric Cornell and Carl Wieman via the cooling and confinement by magnetic fields of a vapor of rubidium-87 atoms [5]. In 2010, Böhl et al. used the coherent manipulation of Bose-condensed atoms in microwave near fields on an atom chip to realize a trapped-atom interferometer with internal-state labeling. Their system enables on-chip generation of many-particle entanglement for quantum sensing and other quantum technology applications [6].

The microwave atom chip in this thesis is based on the design described by William Miyahira in [1]. This microwave atom chip design is formed from microstrip transmission lines, chosen for their small trace widths and spacings and their microwave field mode, which is well suited for generating the field minimums needed in trapping. The microwave atom

chip generates microwave near fields with strong enough gradients to generate a significant AC Zeeman trapping force. Traditionally, atom chips use the DC Zeeman effect to generate a magnetostatic trapping potential. The AC Zeeman effect instead generates spin-specific energy shifts using RF and microwave magnetic fields driven near resonance. This has been demonstrated both theoretically [7] and experimentally [8]. The AC Zeeman trap has been found to suppress potential roughness by several orders of magnitude, when compared to a similar DC Zeeman trap [9]. A major reason atom chips have not been widely adopted is the roughness in magnetic trapping potentials [10], [11].

Simulations of the magnetic field and surface currents on various designs of microwave atom strip (single microstrip, two-microstrip, three-microstrip) have previously been generated in FEKO with inputs of 6.8 GHz with 12.5 W [1]. Thus, this research will explore higher frequency excitations with higher power inputs. This should yield sharper gradients in standing wave near fields, stronger fields, and different coupling behavior.

2.2 Governing Physics

2.2.1 Microstrip Physics

A microstrip consists of a conducting trace separated from a conducting ground plane by a dielectric substrate. Microstrips operate in quasi-TEM (transverse electromagnetic mode), such that the fields exist both in the dielectric and in the air above (Fig. 2.1).

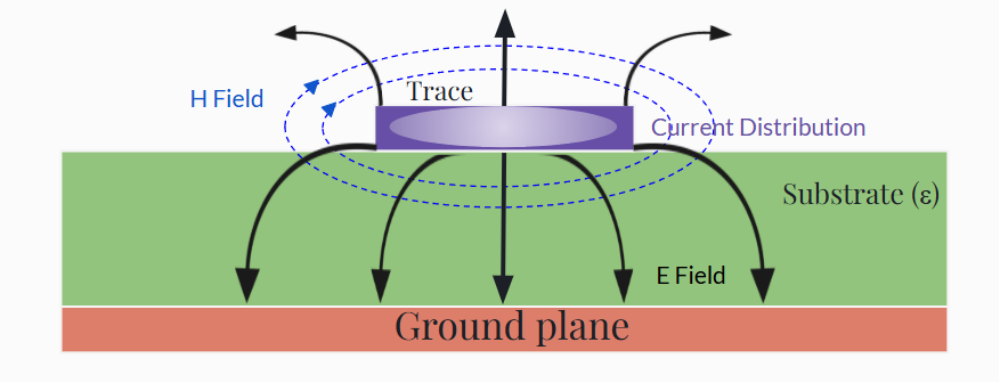

Figure 2.1: Diagram of cross-section of microstrip, showing electric field, magnetic field, and current distribution.

Two microstrips placed near each other (for this model, in parallel) form a coupled transmission line system. Fields from each trace overlap. This system has two modes, the even mode (ϕ=0°, in-phase current) and the odd mode (ϕ=180°, out-of-phase current). The phase ϕ represents the difference in excitation phase between the two traces. This allows for the creation of near-field minima and additional flexibility over the shape of trapping potentials. The two-microstrip structure is also susceptible to crosstalk, which is unwanted coupling between the traces. This can cause power leakage between lines, asymmetrical current distributions, and distorted near-field distributions.

When a wave is propagating in a transmission line, the current as a function of distance z can be found as [12]

$$I(z) = I_o^+ e^{-\gamma z} + I_o^- e^{\gamma z}, \tag{2.1}$$

where the $e^{-\gamma z}$ term represents wave propagation in the $+z$ direction, and the $e^{\gamma z}$ term represents wave propagation in the $-z$ direction.

The complex propagation constant γ is defined as [12],

$$\gamma = \alpha + i\beta = \sqrt{(R + i\omega L)(G + i\omega C)}, \tag{2.2}$$

where R is the series resistance per unit length in Ω/m, L is the series inductance per unit length in H/m, G is the shunt conductance per unit length in S/m, C is the shunt capacitance per unit length in F/m, and β is the phase constant, representing the phase shift of the wave per unit length traveled. The series inductance L gives the total self inductance of the two conductors (the trace and the ground plane) of a mictrostrip. The shunt capacitance C emerges from the proximity of the trace and ground plane. The series resistance R is the result of the finite conductivity of the copper conductors, and the shunt conductance G is the result of dielectric loss in the substrate [12].

From this we can define the characteristic impedance, Z_0 as [12]

$$Z_0 = \frac{R + i\omega L}{\gamma} = \sqrt{\frac{R + i\omega L}{G + i\omega C}}, \tag{2.3}$$

and relate the voltage and current on the line as [12]

$$\frac{V_0^+}{I_0^+} = Z_0 = \frac{-V_0^-}{I_0^-} \tag{2.4}$$

Then (2.1) can be rewritten [12]:

$$I(z) = \frac{V_0^+}{Z_0} e^{-\gamma z} - \frac{V_0^-}{Z_0} e^{\gamma z} \tag{2.5}$$

Then, in the time domain, the voltage waveform is [12]

$$\begin{aligned} v(z,t) = {} & |V_0^+| \cos(\omega t - \beta z + \phi^+) e^{-\alpha z} \\ & + |V_0^-| \cos(\omega t + \beta z + \phi^-) e^{\alpha z} \end{aligned} \tag{2.6}$$

where $\phi^{\pm}$ is the phase angle of the complex voltage $V_0^{\pm}$ [12].

Then, we can find the wavelength on the line [12]:

$$\lambda = \frac{2\pi}{\beta} \tag{2.7}$$

and the phase velocity [12]:

$$v_p = \frac{\omega}{\beta} = \lambda f \tag{2.8}$$

The phase velocity describes the propagation speed of a fixed phase of the wave. In a parallel microstrip geometry, coupling between adjacent traces affects how strongly the electromagnetic fields interact with the dielectric substrate, which in turn changes the phase velocity. Thus, in coupled microstrips, the even and odd modes tend to propagate at different velocities. Generally, odd mode propagation is slower. In odd mode operation, more field concentrates in the substrate, and the effective dielectric constant becomes larger. In a low-loss system,

$$v_p = \frac{c}{\sqrt{\epsilon_e}} = \lambda f, \tag{2.9}$$

where ϵ_e is the effective dielectric constant of the microstrip line [12]. As the field extends into both the dielectric substrate and the air surrounding the copper trace, ϵ_e depends on the substrate's dielectric constant, the substrate thickness, the trace and ground plane width, and the frequency [12].

A microwave lattice on a parallel microstrip structure is a periodic network where the chip geometry and excitations used create a pattern of high field concentration and nodes along the traces, which is shifted by one node between the traces. A node on one trace should line up with an area of high field concentration on the other trace. This is predicted to be

achievable using two long parallel microstrips at high frequency, out of phase by $\phi = 180°$. A microwave lattice yields finer control over how the wave propagates through the device and greater ability to shape the magnetic field to the exact specifications needed for atom trapping and interferometry.

2.2.2 Finite Element Method

Ansys HFSS uses the finite element method (FEM), a numerical technique for solving differential equations in mathematical modeling. FEM is typically used to solve partial differential equations of 2 or 3 space variables. This holds true for its use in Ansys HFSS. The FEM procedure first divides a structure into many smaller subsections, called finite elements. In HFSS, these finite elements are called tetrahedra, and the entire collection of tetrahedra within the structure is called a mesh. A solution for the fields is then found within each of the tetrahedra. Then, the fields between each adjacent finite element is interconnected such that Maxwell's equations are satisfied across the inter-element boundary. This generates an electromagnetic field solution for the entire structure. From the field solution, the generalized S-matrix solution (the method through which Ansys HFSS computes the S-parameters) is determined [13].

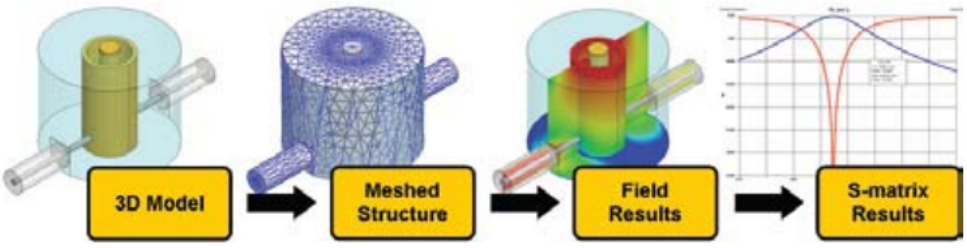

Figure 2.2: Visualization of the finite element method, from [13].

2.2.3 Electromagnetic Solution

Ansys HFSS solves for the electric field (**E**) and magnetic field (**H**) using the following equations [13]:

$$\nabla \times \left(\frac{1}{\mu_r} \nabla \times \mathbf{E} \right) - k_0^2 \epsilon_r \mathbf{E} = 0 \tag{2.10}$$

where $\mu_r = \frac{\mu}{\mu_0}$, $\epsilon_r = \frac{\epsilon}{\epsilon_0}$, $k_0^2 = \omega^2 \epsilon_0 \mu_0 = \frac{\omega^2}{c^2}$

$$\mathbf{H} = \frac{j}{\omega \mu} \nabla \times \mathbf{E} \tag{2.11}$$

Appropriate boundary conditions and excitations are applied accordingly to the model. Other electromagnetic quantities are derived from the solved fields. In this way, Ansys HFSS operates completely through the framework of electric and magnetic fields. This is ideal for the case of microstrips, for which the operational principal is that electromagnetic fields are guided along the interface of a metal and dielectric.

2.2.4 Thermal Solution

For the conducting microwave traces, the temperature is predominantly determined by Joule heating. Through the process of Joule heating, current passing through a conductive material generates heat. When current flows through a material with a finite resistance, electrical energy is dissipated as heat. The resulting increase in temperature can subsequently increase the material's resistance.

The Joule heating on a conductor surface can be represented by the conductive power loss P_s, as given by [14]:

$$P_s = \frac{1}{2} \int_S R_s |\mathbf{H}_{tan}|^2 ds \quad \text{[W]} \tag{2.12}$$

Where the surface resistance R_s is:

$$R_s = \sqrt{\frac{\omega\mu}{2\sigma}} = \frac{1}{\sigma\delta} \quad [\Omega] \tag{2.13}$$

In these equations,

- $\mathbf{H}_{tan}$ is the tangential magnetic field at the surface
- ω is the angular frequency ($2\pi f$)
- μ is the magnetic permeability of the conductor
- σ is the electrical conductivity
- δ is the skin depth $\delta = \sqrt{\frac{2}{\omega\mu\sigma}}$

The equation for the power dissipated per unit surface area of the conductor due to surface currents is,

$$q_s = \frac{1}{2} R_s \left| H_{\tan} \right|^2 \quad [\mathrm{W/m^2}] \tag{2.14}$$

where Fourier's law can be combined with the principle of energy conservation to yield the steady state heat conduction equation with internal heat generation,

$$\nabla \cdot (k \nabla T) + q = 0 \tag{2.15}$$

with k being thermal conductivity in W/m·K and q being volumentric heat in $\mathrm{W/m^3}$.

From this series of equations, the gradient of the temperature field, ∇T is calculated.

$$\nabla T = \left(\frac{\partial T}{\partial x}, \frac{\partial T}{\partial y}, \frac{\partial T}{\partial z} \right) \tag{2.16}$$

2.2.5 S-Parameters

For microstrips, S-parameters (scattering parameters) are used for assessing impedance matching (to the characteristic impedance Z_0=50 Ω) and assessing signal integrity. They determine how waves propagate, reflect, and transmit between the two ports at each end of the strip. S-parameters are complex numbers used to represent both the complex and frequency-dependent aspects of the wave (i.e., both magnitude (dB) and phase). From these values, device behavior can be analyzed. S-parameters are generally given as S_{ij}, where index i is the "end" port and the index j is the input/excited port.

S_{11} is the reflection coefficient, or return loss, at port 1. It measures how much energy is reflected back to the excited port 1. A reflection coefficient of $\leq$ -20 dB or greater corresponds to reflected energy of less than 1% and is considered an optimal impedance match. This yields the best signal purity and overall performance. A reflection coefficient $\leq$ -10 dB is considered barely acceptable. A range of -15 to -20 dB is generally targeted as "good" performance.

S_{21} is the transmission coefficient, or insertion loss. It measures how much energy is transmitted from port 1 to port 2. For the substrate material aluminum nitride (AlN) used in this model, the ideal average insertion loss should be <0.5 dB/mm [15].

The S-parameters are mathematically determined in the model using the following sequence of equations. The modal representation of the electric and magnetic fields at each

port, assuming K modes, are [16]:

$$\mathbf{E} = \sum_{m=1}^{K} (a_m + b_m)\mathbf{e}_m \tag{2.17}$$

$$\mathbf{H} = \sum_{m=1}^{K} (a_m - b_m)\mathbf{h}_m \tag{2.18}$$

Here, a_m and b_m are unitless complex amplitudes of the incident and reflected modal fields, respectively. S-parameters can be further categorized in terms of the incident and reflected/transmitted modal amplitudes using the generalized S-matrix $\mathbf{S}$ [16]:

$$\mathbf{b} = \mathbf{S}\mathbf{a} \tag{2.19}$$

Here, $\mathbf{a}$ and $\mathbf{b}$ are unitless complex modal coefficient vectors. N (the size of the vector) is the total number of modes obtained by adding up the number of modes of all ports [16]. For this model, all ports had 1 mode.

Each entry of the S-matrix, S_{ij}, gives the multiplication factor that is applied to the incident modal amplitude a_j. The product is the reflected/transmitted modal amplitude b_i (in the case where all the other incident modes are off). For an index variable k, this can be written [16]:

$$S_{ij} = \left.\frac{b_i}{a_j}\right|_{a_k=0,\, k\neq j} \tag{2.20}$$

2.3 Approximations and Assumptions

2.3.1 Mesh Refinement and Solution Validity

Ansys HFSS determines mesh refinement based on the value set for Maximum Delta S (ΔS). ΔS is defined as the magnitude of the change of the S-parameters between two consecutive passes. The Maximum Delta S value serves as the stopping criterion for the adaptive solution. Once the magnitude of the change between all S-parameters from one iteration to the next is less than the Maximum Delta S value, the adaptive analysis will stop. Otherwise, it will continue to complete passes until either the criterion is met or the maximum requested number of passes (in this case, 99) is met [17]. The Maximum Delta S value is chosen to be small enough for optimal accuracy (which can be determined by plotting the resulting mesh), but not so small that the simulation will overwhelm the computer or fail to resolve in reasonable time. The formula for Maximum Delta S is [18]:

$$\max_{i,j} \left| S_{ij}^{N} - S_{ij}^{N-1} \right| \tag{2.21}$$

For the simulations in this research, a Maximum Delta S value of 0.005 was used for smaller models and a Maximum Delta S value of 0.01 was used for larger models. In each case, the number of adaptive passes was set high enough that every solution converges. The mesh of each model was plotted to ensure that the generated mesh was fine enough to support physically realistic solutions. A length-based mesh size of a quarter of the microstrip width ($\frac{1}{4} \times 54$ µm) was defined for the microwave traces. The appropriate meshing resolution for the rest of the model was determined based off this minimum resolution value.

2.3.2 Boundary Conditions

The boundary of the model is defined to resemble an unbounded domain which absorbs any outgoing electromagnetic radiation. Within the simulation, this takes the form of an air box above the substrate, which is set to be a radiation boundary. For thermal simulations, the bottom plane of the ground plane was set as a temperature boundary of 20°C, and the other outer edges of the ground plane were made to form a convection boundary. The substrate and traces also had convection boundaries applied. The convection boundary, which defines the heat dissipation on surfaces exposed to air, was 1 W/(m^2· K) in all cases. This value defines the convection film coefficient, and is associated with negligible cooling. A convection boundary of 1 W/(m^2· K) models very weak convection, but is not accurate to true vacuum physics. Ideally, the thermal simulations would be run again in true vacuum with a convection boundary of 0 W/(m^2· K).

2.3.3 Microstrip Model Validation

S-Parameters of the solved model are checked to ensure they fall within the specifications outlined in section 2.2.5 for good quality. The mesh is plotted on the model to ensure it is fine enough.

Chapter 3

Methodology

3.1 Model Overview

The basic model used in this work (Fig. 3.1) is a 5 mm x 7 mm chip. It consists of two parallel microwave traces of 5 µm thick copper on a 50 µm aluminum nitride (AlN) substrate with a dielectric constant of $\epsilon_{AlN} = 8.9$ and a thermal conductivity of 120 W/(m·K). This is on top of a 1 mm thick copper ground plane. An especially thick ground plane is chosen for reduced resistive losses and improved heat dissipation, when compared to design with a thin ground plane. Copper is used in this simulation, as opposed to a perfect electric conductor, for the greatest accuracy to a real physical atom chip.

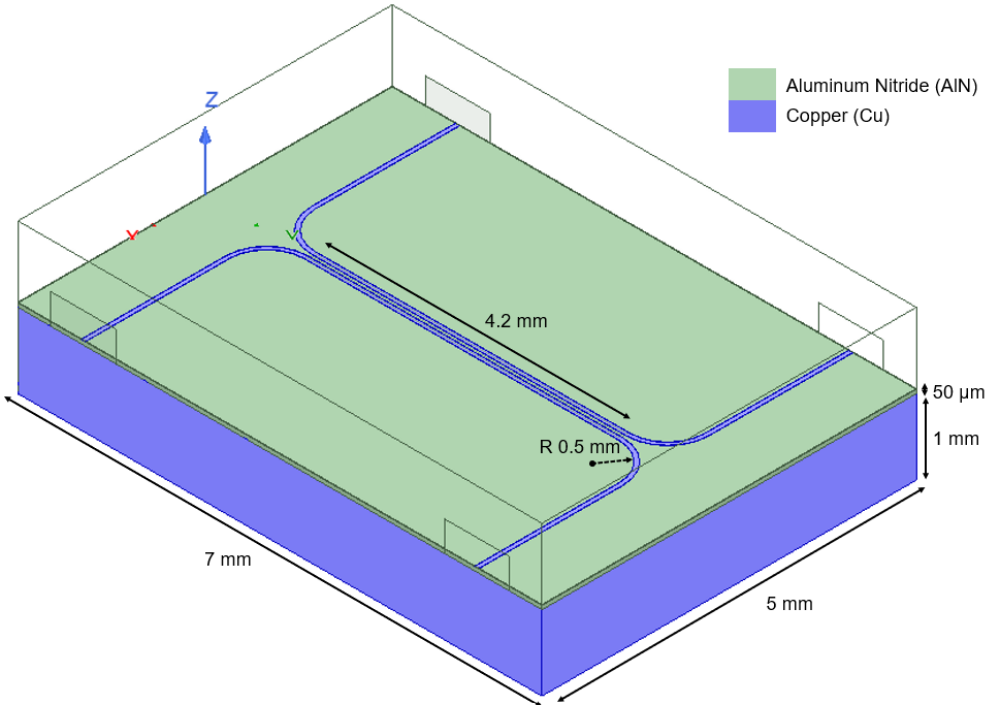

Figure 3.1: Model of standard chip with two parallel 4.2 mm long microwave traces, each with 50 Ω characteristic impedance.

Each of the microwave traces are curved towards the long edge of the chip, perpendicular to the layout they assume when parallel to each other. The curved section ends 1.4 mm from the shorter edge of the chip. This curve is constructed as a segment of a circle, with its inner radius being 0.5 mm. This makes it so that for the 5 mm x 7 mm chip, the parallel microstrips are actually 4.2 mm $(7 - 2 \times 1.4)$ in length. This design feature was chosen due to the physical set-up. A coaxial cable with a diameter of 380 µm connects the microwave amplifier, which provides the signal input, to the copper traces on the chip. Field interactions between the traces drive the functionality of the microwave atom chip, so the traces must be sufficiently close to each other. The incorporation of a curve allows the traces to be very close to each other without any complications caused by coupling to the coaxial cables. In this model, each trace is 54 µm across, and the gap between the two traces is 100 µm center-to-center, or 46 µm edge-to-edge (Fig. 3.2). The trace is 5 µm, the substrate is 50 µm thick, and the ground plane is 1 mm thick. Each trace has an impedance of 50 Ω.

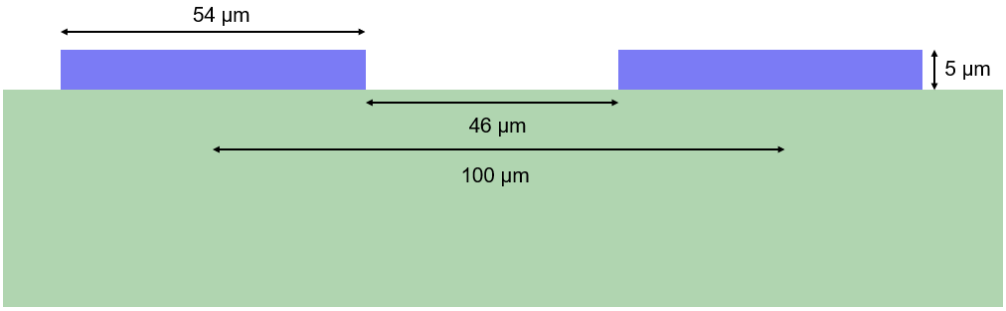

Figure 3.2: Diagram of cross-section of standard chip with two parallel microwave traces.

3.2 Design Variations

Variations of the base model of the chip are used to probe and evaluate certain behaviors. The first alternate design is the single microstrip chip (Fig. 3.3), which possesses all the same dimensions as the base model, but has only one microwave trace. This model is used primarily to draw comparison to the double microstrip models.

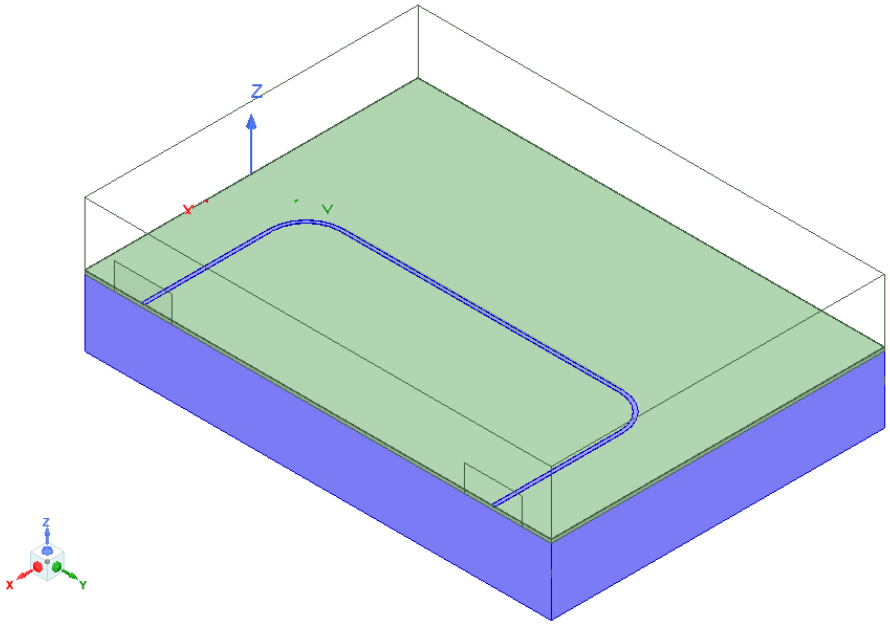

Figure 3.3: Model of chip with single 4.2 mm long microwave trace.

The second design variation used in this work is an ultra-long chip (Fig. 3.4), which has 24 mm long microwave traces. This design is used to observe electromagnetic energy transfer between traces, current maxima along the traces, and standing wave patterns. In particular, this model is used in attempts to visualize a microwave lattice.

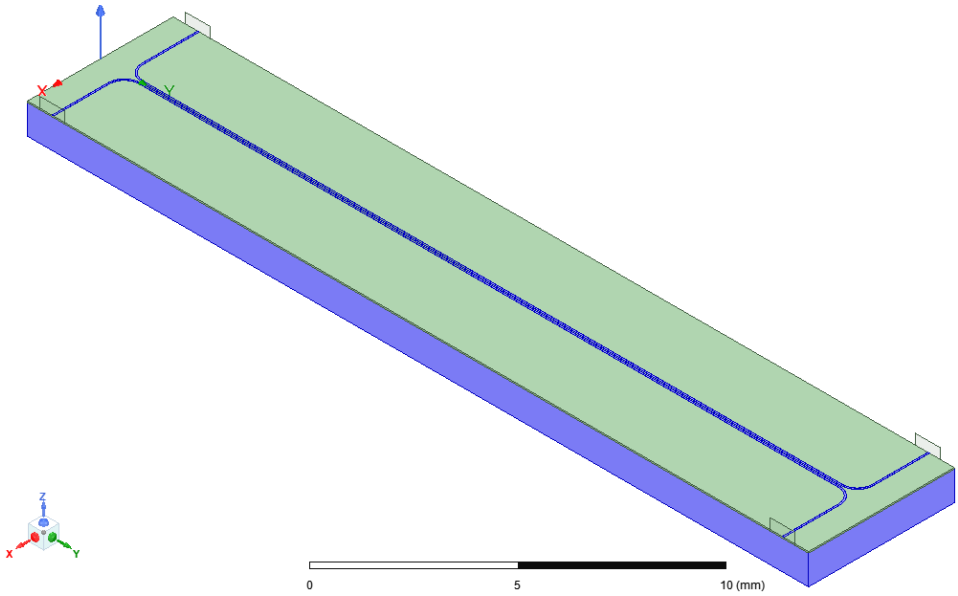

Figure 3.4: Model of chip with two parallel 24 mm long microwave traces, each with a 50 Ω characteristic impedance.

3.2.1 Simulation Setup

The simulations described in this thesis are all conducted in Ansys HFSS using the Driven Modal Solution Type. Each trace in the model has two excitations, which are wave ports on each end of the trace. These ports are defined by a two-dimensional surface constructed perpendicular to the end of the trace. The height of the wave port must be ≥5h, where h is the thickness of the substrate. The width must be ≥5w, where w is the width of the microstrip. The bottom of each wave port is aligned with the bottom edge of the substrate. Each port is defined to support 1 mode and have Zpi characteristic impedance. Ansys HFSS can calculate characteristic impedance in a variety of ways. For this model, it is calculated

using the formula [19]:

$$Z_{PI} = \frac{P}{I^2} \tag{3.1}$$

Both power and current are computed directly from the simulated fields. The power flow through the port is calculated using the following equation, integrated over the surface of the port [20]:

$$W = \oint_S \mathrm{Re}(\mathbf{P}) \cdot \mathbf{n}\, dS \tag{3.2}$$

For the complex Poynting vector $\vec{P}$:

$$\mathbf{P} = \frac{1}{2}\, \mathbf{E} \times \mathbf{H}^* \tag{3.3}$$

where $\mathbf{E}$ is the electric field, $\mathbf{H}$ is the magnetic field, and $\mathbf{n}$ is the unit vector normal to the surface.

Current is computed by Ampere's Law:

$$I = \oint_l \mathbf{H} \cdot d\mathbf{l} \tag{3.4}$$

Each port is normalized to an impedance of 50 Ω. For an activated port, a 20 W power input is used.

The boundary of the model is defined by an air box above the substrate, which is set to be a radiation boundary. This simulates an unbounded domain by absorbing any outgoing electromagnetic radiation.

3.3 Simulation Protocol

The simulation protocol differs slightly based on whether it is being run for the smaller chip or the ultra-long chip.

For the smaller chip, the following parameters are varied:

1. Number of excitations (single trace v. dual trace)
2. Excitation frequency (6.8 GHz v. 15 GHz)
3. Phase difference between traces (0° v. 180°)

When evaluating single trace excitation, only 1 port is activated (at 20 W and either 6.8 or 15 GHz). 6.8 GHz is the ground state hyperfine splitting frequency of rubidium-87, and thus very commonly used in physics labs. 15 GHz is chosen as a "high" frequency, used to evaluate whether certain behaviors change or becomes more visible at higher frequency. In the case of single excitation, the leaking of energy into the inactive trace and the resulting crosstalk is of interest.

For dual trace excitation, two ports directly across from each other on the model are activated (at 20 W and either 6.8 or 15 GHz). This enables the study of modal behavior in the system. A 0° phase difference represents the even mode, in which current flows in the same direction along both traces. A 180° phase difference represents the odd mode, in which current flows in opposite directions across the traces. The phase difference between excitations is set as a parameter in Ansys HFSS, defined with other input specifications, such as power.

Both an electromagnetic and thermal simulation is run for each case. The solved model from the electromagnetic simulation is imported into Ansys Mechanical, and a link to the

original solved model's meshing and solution is generated to find the thermal solution. In the electromagnetic simulation, the current and magnetic field of the chip are observed. In the thermal simulation, the temperature along the traces is observed. Surface current contributes to heating on the microstrips ($P = I^2R$), and that raised temperature raises resistivity. The electromagnetic and thermal properties of the chip are directly related.

Ansys HFSS automatically generates a mesh based on the solution frequency setup and convergence criteria. For the smaller model, a $\Delta S = 0.005$ convergence criterion was used. This makes the maximum change in S-parameters between passes 0.5%. This value ensures numerical stability and accuracy of both the amplitude and phase of the magnetic field. A maximum of 99 adaptive passes was allowed, to ensure convergence.

For the ultra-long chip, the following parameters are varied:

1. Excitation frequency (15 GHz v. 30 GHz)

For this chip, the specific interest is to observe energy transfer between traces and generate a microwave lattice. In this case, only one excitation is necessary. In a similar vein, as this behavior is easier to achieve and identify at higher frequency, only higher frequencies are probed. A thermal simulation was not run for this case.

For the ultra-long model, $\Delta S = 0.01$ was used. This makes the maximum change in S-parameters between passes 1%. This value is larger than that used for the smaller model simply because the larger model is much more computationally intensive to run. This ΔS accuracy should adequately capture the magnetic field amplitude and phase. Again, a maximum of 99 adaptive passes was allowed to ensure convergence.

3.4 Data Acquisition

Within Ansys HFSS, reference lines for measurements were drawn running parallel to the traces. Two (or one, for the single strip model) were drawn on the top surface of the copper traces, and one was drawn between the two traces, on the surface of the substrate. Current and temperature are plotted as functions of distance x along each of the lines.

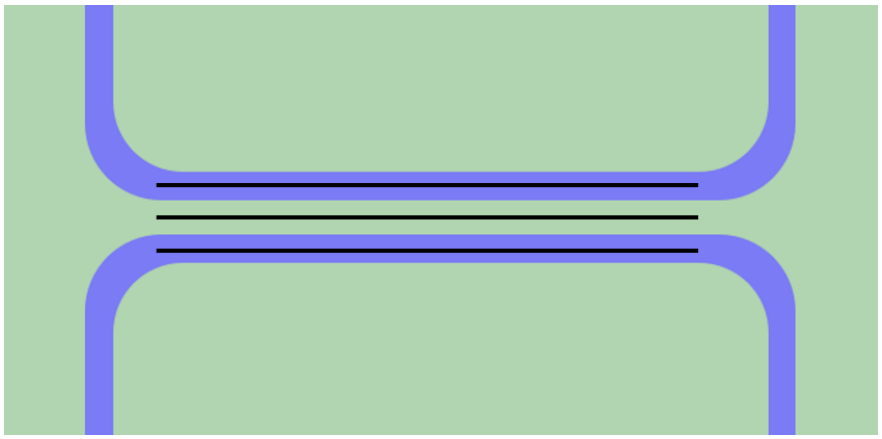

Figure 3.5: Graphic showing positions of reference lines (shown in in black) that values were plotted along.

A plane 5 µm above the top surface of the traces is used to visualize the magnetic field. At the surface of a conductor, magnetic field quantity is mainly tied to surface current,

$$\mathbf{H} = \mu_o \mathbf{J} \tag{3.5}$$

where $\mathbf{J}$ is the surface current. Then, it is necessary to look at the magnetic field a distance above the copper traces to get a "clean" image. Current is plotted directly on the copper traces.

Chapter 4

Results

Ansys HFSS simulations were run to observe magnetic field, current, and heating on the chip. First, a single trace model with a 4.2 mm long trace is evaluated with both 6.8 GHz and 15 GHz. Current and magnetic field along the trace are plotted. Next, simulation results of the chip with two parallel 4.2 mm long traces are shown. This simulation is solved with both single excitation at one port and dual excitation at two parallel ports. Magnetic field and current are plotted for the single excitation case. Magnetic field, current, and heating are plotted for the dual excitation case. For dual excitation, both even and odd modes are solved for. The simulation is solved at both 6.8 GHz and 15 GHz input power. A large scale atom chip model with 24 mm traces is used to assess field and current transfer between two adjacent traces. For the large scale case, excitation frequencies of 6.8 GHz and 15 GHz are used at only one input port (single excitation). Magnetic field and current are plotted on the chip. For all simulations, 20 W input power is used at excited ports. All non-excited ports are terminated at 50 Ω impedance.

4.1 Single Trace Model

In the single trace model, both 6.8 GHz excitation and 15 GHz excitation with 20 W input power is probed to see how the behavior of currents and fields changes between frequencies.

4.1.1 6.8 GHz Input

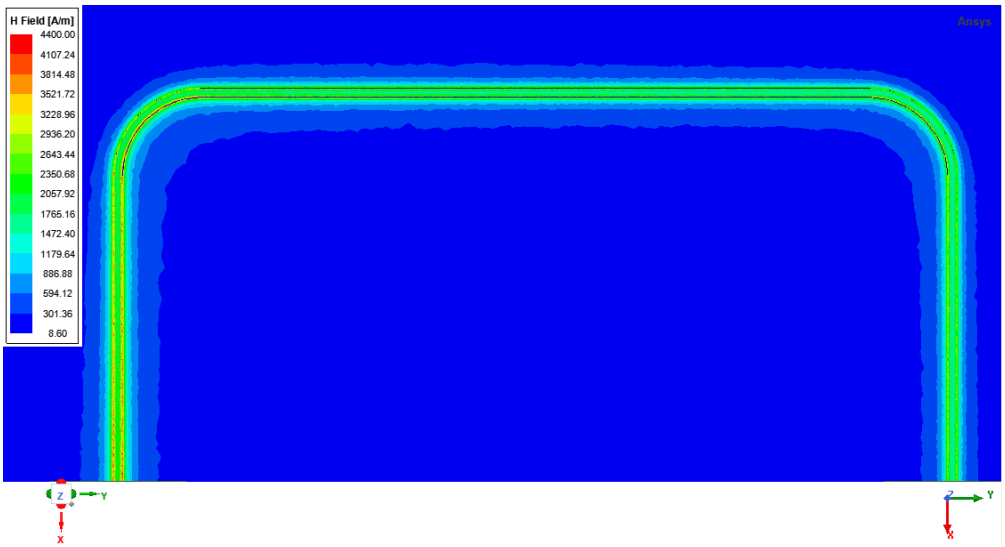

Figure 4.1: Magnetic field distribution from a 6.8 GHz input signal at left port plotted above a single microwave trace.

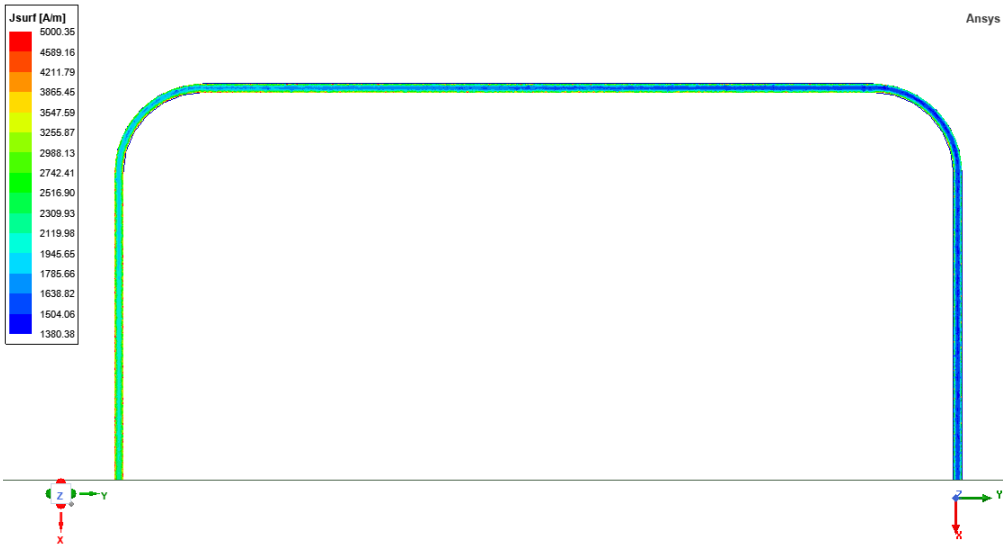

Figure 4.2: Current density distribution from a 6.8 GHz input at left port signal plotted on a single microwave trace.

The magnetic field and current (Fig. 4.1 and 4.2, respectively) are stronger and more concentrated along the edges of the trace due to the AC skin effect. It can be observed that the current prefers the inner edge of curves from the greater edge concentration there. It can also be observed that the current and field dissipate along the trace.

4.1.2 15 GHz Input

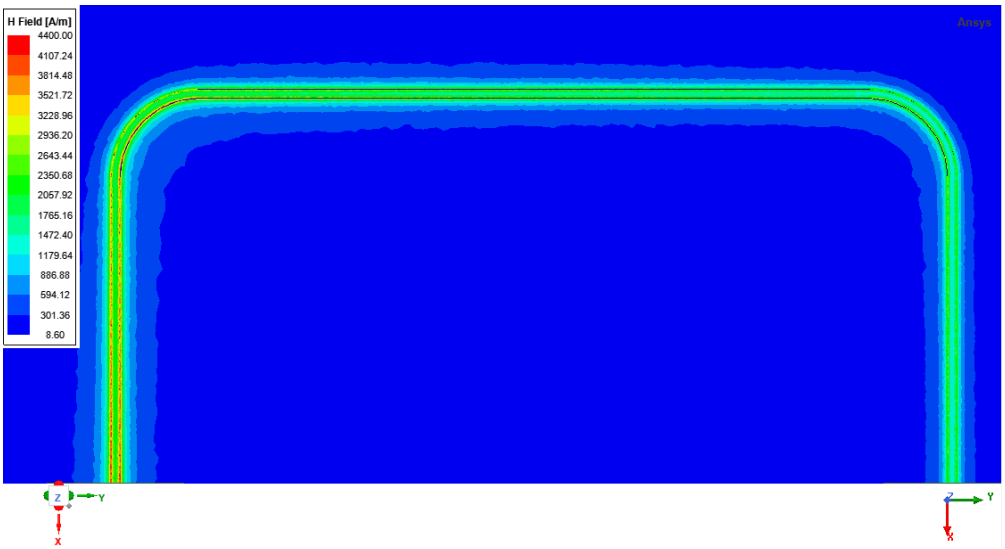

Figure 4.3: Magnetic field distribution from a 15 GHz input signal at left port plotted above a single microwave trace.

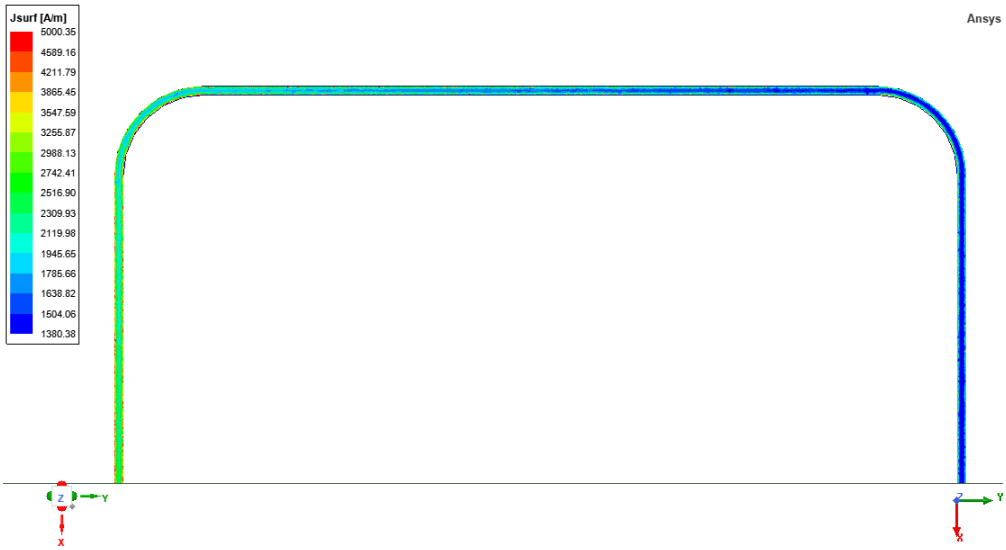

Figure 4.4: Current density distribution from a 15 GHz input signal at left port plotted on a single microwave trace.

The magnetic field and surface current at 15 GHz (Fig. 4.3 and 4.4) look very similar to those at 6.8 GHz (Fig. 4.1 and 4.2), with slightly higher values at the trace's edges.

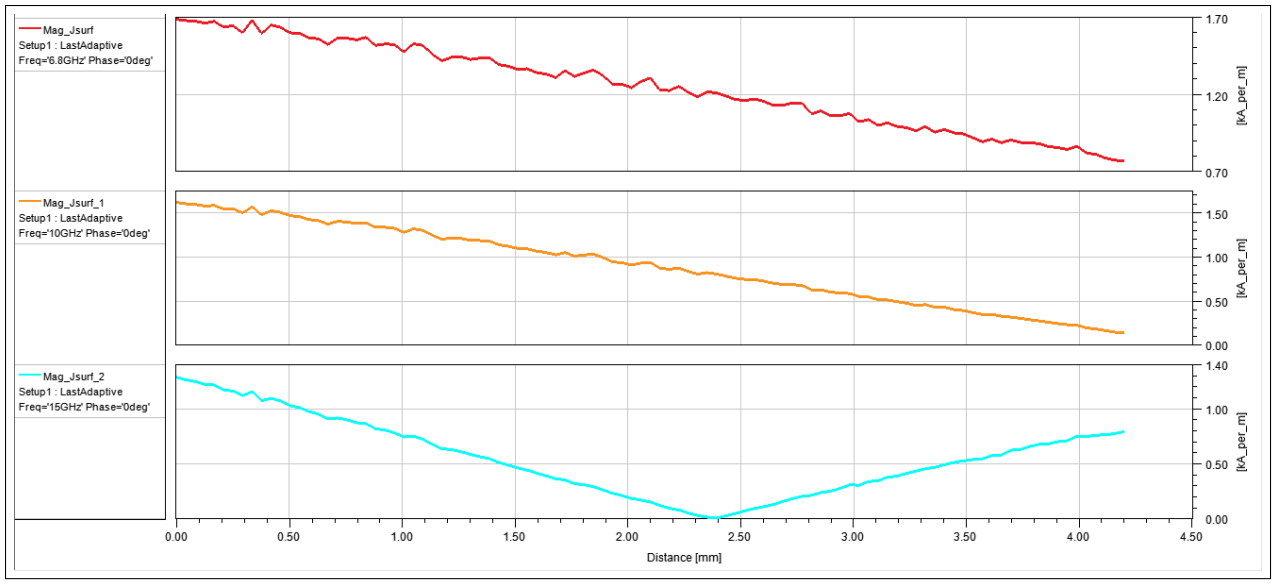

Figure 4.5: Magnitude of surface current density from a 6.8, 10, and 15 GHz (top, middle, and bottom, respectively) input signal plotted as functions of distance along length of trace.

The current at 6.8 GHz and 10 GHz (tested as an intermittent frequency in this model) follow a similar downward trajectory along the length of the trace. The current for the 15 GHz model, however, decreases and reaches a minimum at zero, and then again increases. In Fig. 4.5, the full complex magnitude $|\mathbf{J}|$ for $|\mathbf{J}| = \sqrt{J_{real}^2 + J_{imag}^2}$ is plotted. The minimum of the surface current density appears to hit in Fig. 4.5 is not a true minimum, but rather the point at which the surface current density changes sign (in this case, phase orientation). The current from the 15 GHz signal changes sign at a distance of x = 2.4 mm on the straight segment of the trace (Fig. 4.5).

4.2 Small Scale Two-Trace Model

4.2.1 Single Trace Excitation

For the 4.2 mm long two-trace model, a single transmission line is excited at 15 GHz to observe interactions between the excited and unexcited microstrips. This simulation is run at 15 GHz using the 4.2 mm long model, and will later be used to draw comparisons to the same set-up in the 24 mm trace model.

15 GHz Input

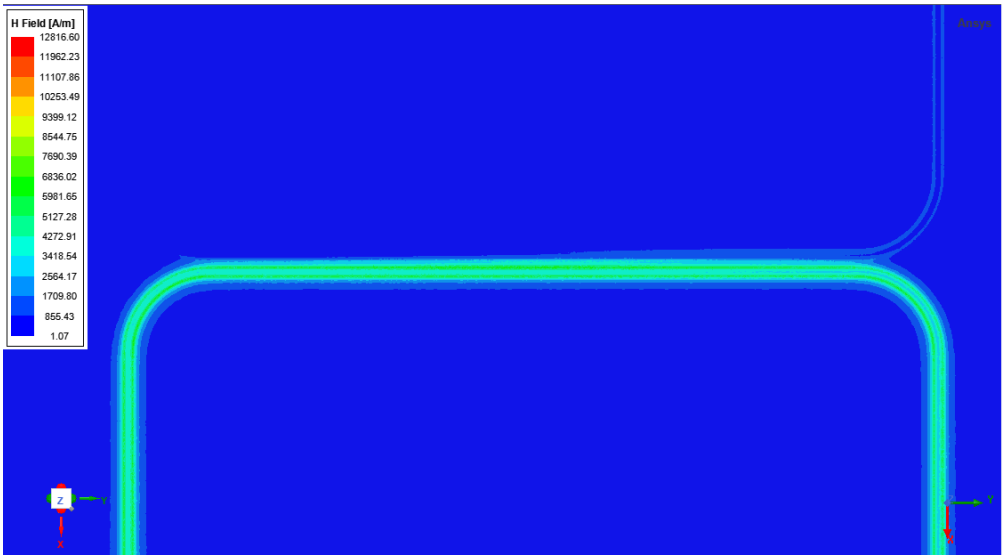

Figure 4.6: Magnetic field distribution from single 15 GHz input signal at bottom left port plotted above two parallel microwave traces.

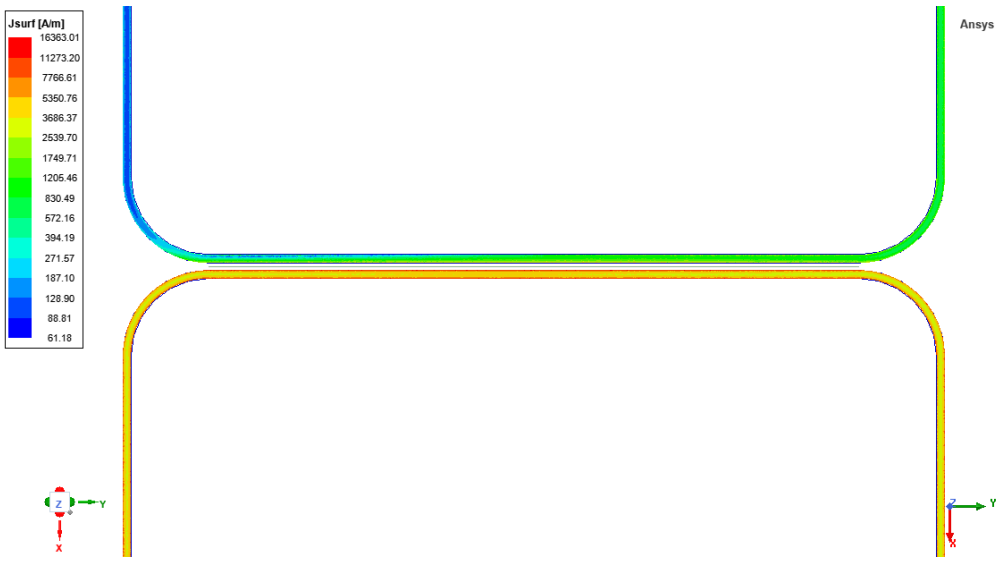

Figure 4.7: Current density distribution from single 15 GHz input signal at bottom left port plotted above two parallel microwave traces.

In Fig. 4.6 and 4.7, the field distribution and current density, respectively, partly migrate to the inactive trace.

4.2.2 Dual Trace Excitation ($\phi = 0\ ^\circ$)

The two-trace model is now excited at two ports directly across from each other, on opposite traces. The first simulation will be in the even mode, for which both currents travel in the same direction (see Fig. 4.8).

As previous models have shown current to be analogous to the magnetic field, its plot on the chip will not be shown for the following simulations.

6.8 GHz Inputs

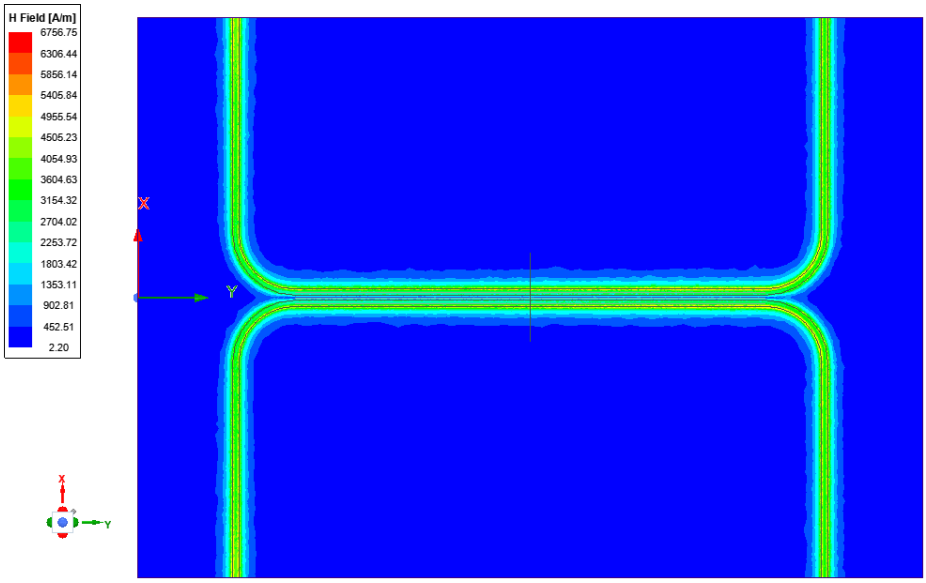

Figure 4.8: Magnetic field distribution from parallel 6.8 GHz input signals ($\phi = 0°$) at top and bottom left ports plotted above two parallel microwave traces.

It is shown in Fig. 4.8 and Fig. 4.9 that the field concentrates most strongly on each outer edge of each transmission line. When the microstrips are parallel, with parallel current flowing, the field overlap between the two traces makes it appear as if it were a single, bigger trace.

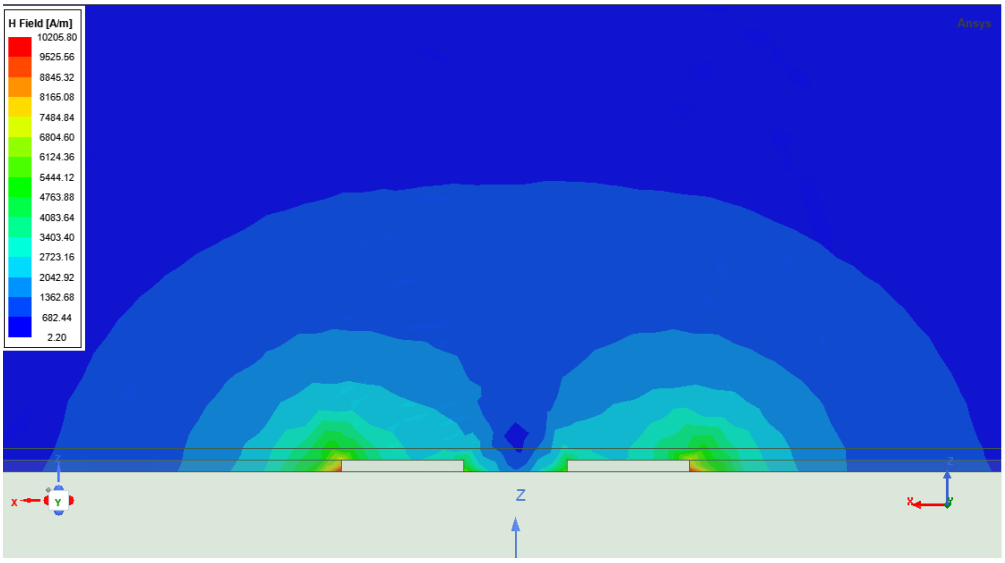

Figure 4.9: Magnetic field distribution from parallel 6.8 GHz input signals ($\phi = 0°$) plotted at central cross-section of two traces and substrate.

At the cross-section, it is evident that the field distribution concentration hugs the outer edges (Fig. 4.9). There is also an increase in distribution on the inner edge, which is a remnant of the traditional skin effect for a singular trace. The magnetic field minimum is in the center between the two traces, 15 µm above the substrate. This field minimum is the atom trap.

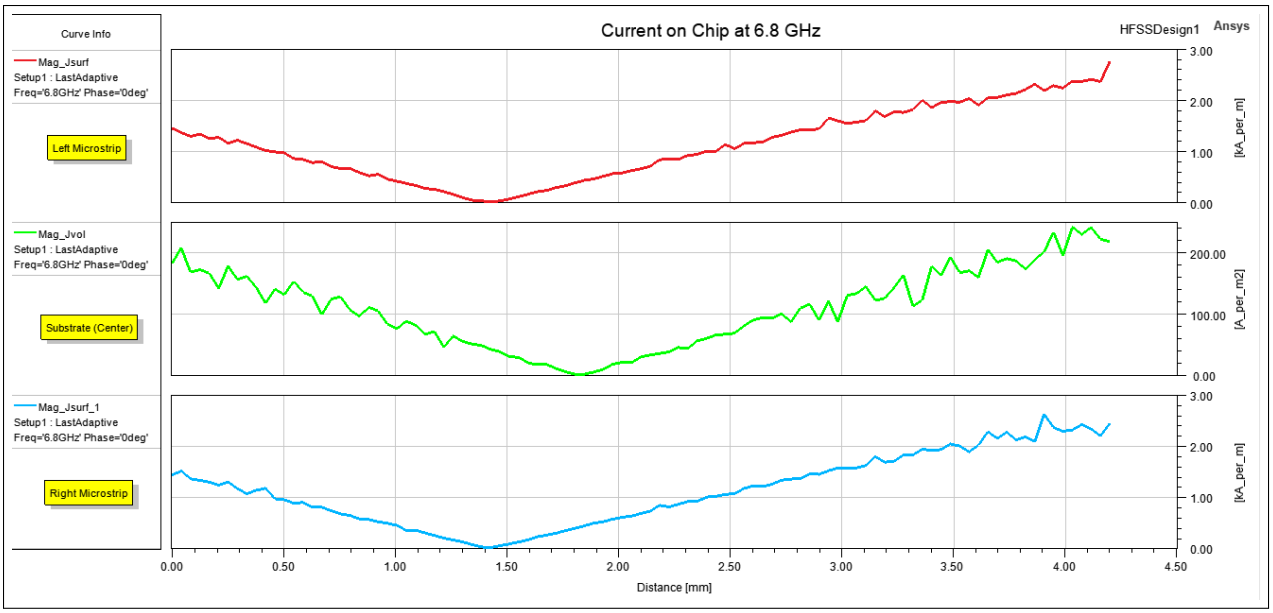

Figure 4.10: Magnitude of current density from parallel 6.8 GHz input signals ($\phi = 0°$) plotted as functions of distance along length of both traces and center line.

The surface currents in the left (bottom) and right (top) (as oriented in figure 3.1) microstrips are plotted as a function of distance on the trace. The volumetric current in the substrate between the traces is also plotted, for comparison and assessment of current leakage into the dielectric substrate. The current minimum on either strip is at z = 1.4 mm.

Now, for this model, thermal quantities were also solved for, as shown in Fig. 4.11 and 4.12. A thermal conductivity of 120 W/(m·K) was used for the AlN substrate.

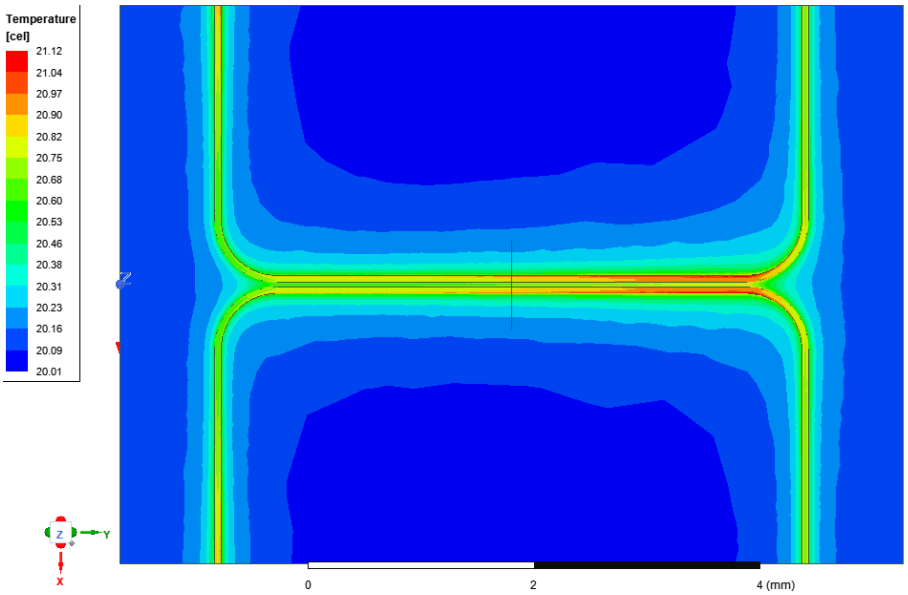

Figure 4.11: Temperature from parallel 6.8 GHz input signals ($\phi = 0°$) at top and bottom left ports plotted above two parallel microwave traces.

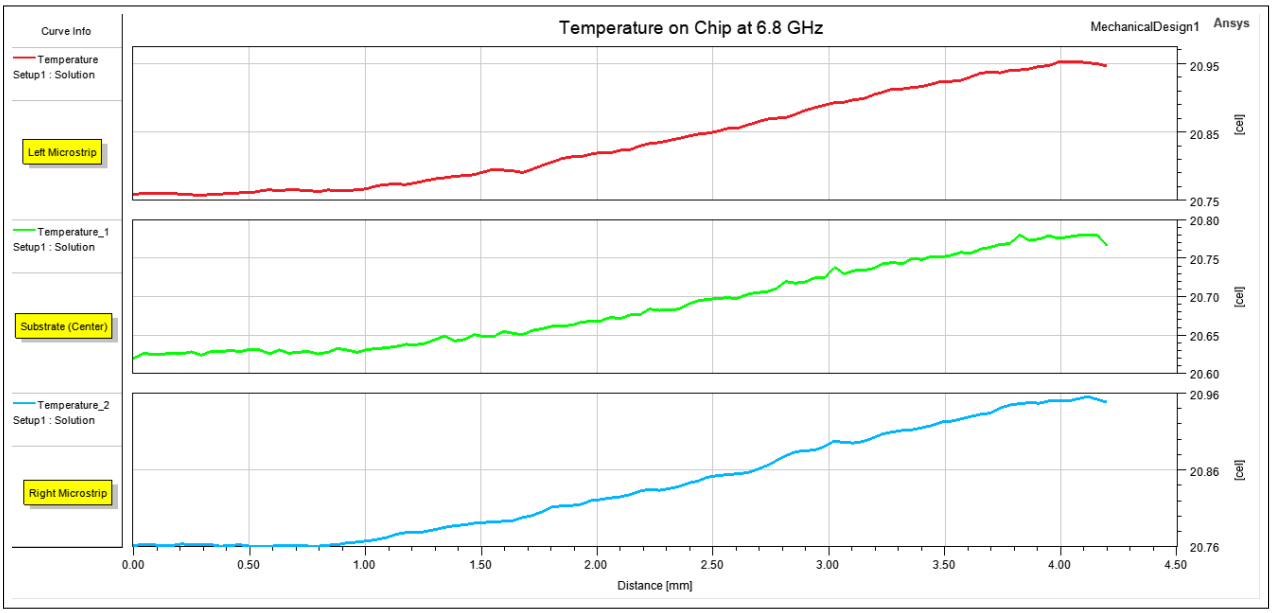

Figure 4.12: Temperature from parallel 6.8 GHz input signals ($\phi = 0°$) at top and bottom left ports plotted as functions of distance along length of both traces and center line. Total $\Delta T = 0.20°C$ for each microstrip.

The highest temperature is at the end of the traces, corresponding to where the highest current was found. Reflections occur at this second curve, causing current to concentrate

there. The temperature variation is symmetric across traces, and peaks at 20.95°C (Fig. 4.12).

15 GHz Inputs

At 15 GHz, the behavior induced by skin effect is much more visible (see Fig. 4.13 and 4.14).

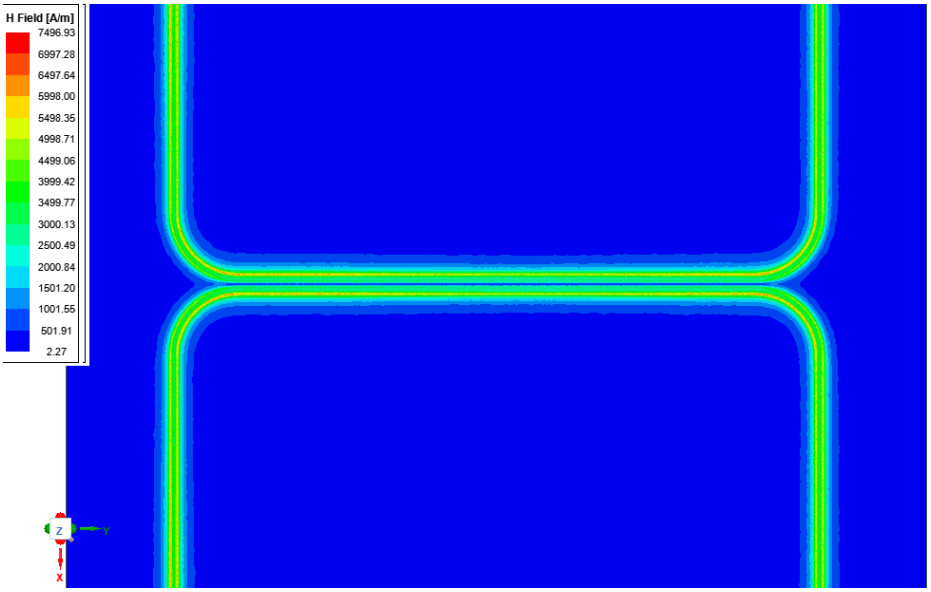

Figure 4.13: Magnetic field distribution from parallel 15 GHz input signals ($\phi = 0°$) at top and bottom left ports plotted above two parallel microwave traces.

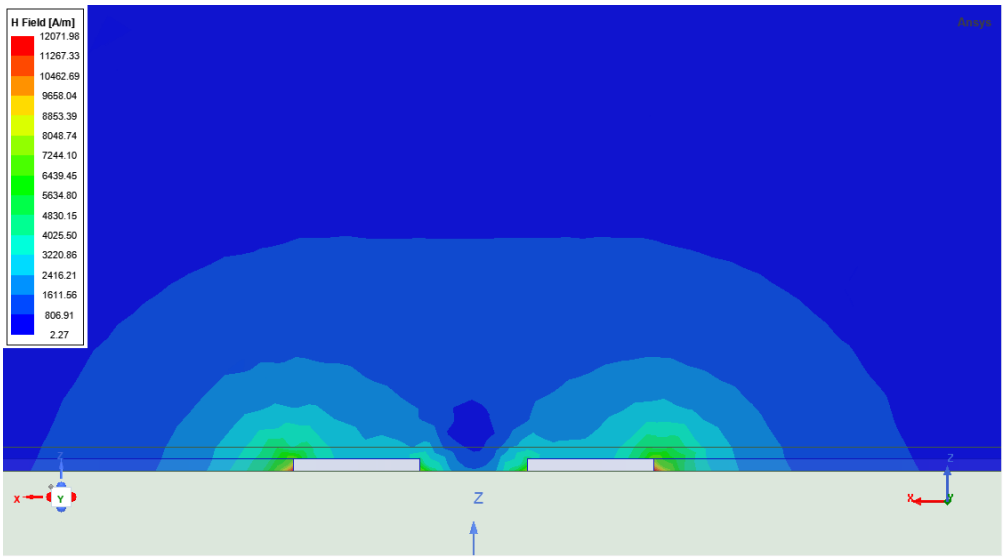

Figure 4.14: Magnetic field distribution from parallel 15 GHz input signals ($\phi = 0°$) at top and bottom left ports plotted at central cross-section of two traces and substrate.

The minimum in the magnetic near field is located in the middle of the chip, 15 µm above the substrate again (see Fig. 4.14). When plotted along the reference lines, the current profile begins to look like a periodic curve (see Fig. 4.15).

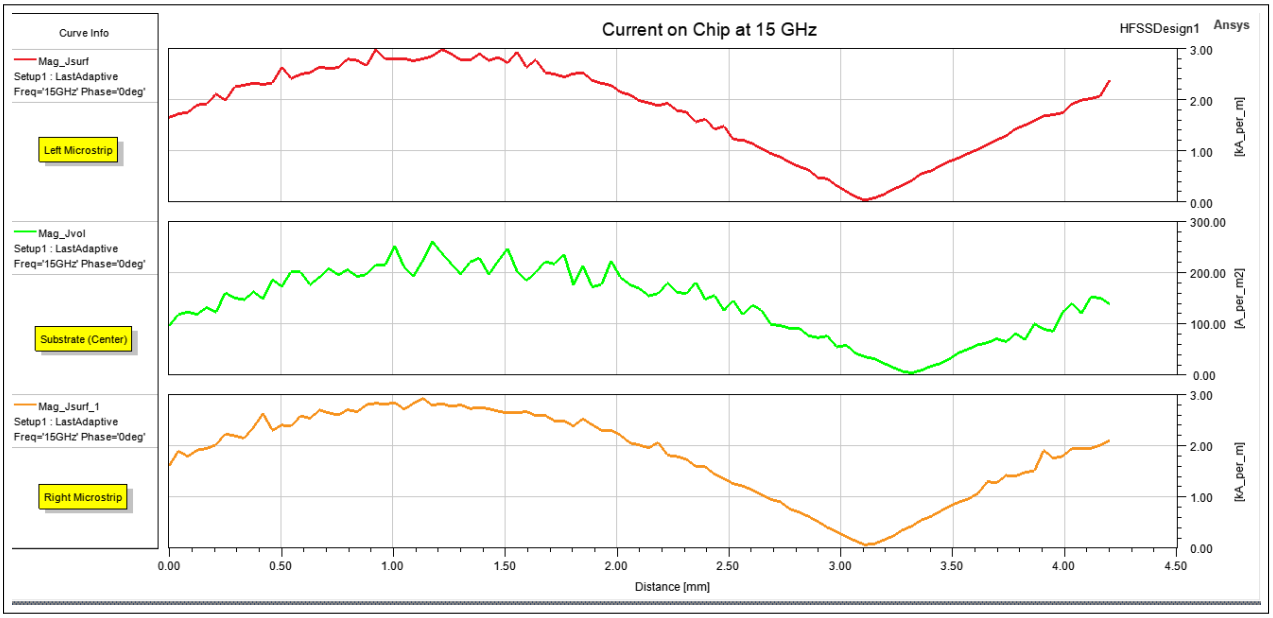

Figure 4.15: Magnitude of current density from parallel 15 GHz input signals ($\phi = 0°$) plotted as functions of distance along length of both traces and center line.

Now, the thermal quantities for this model are solved for (Fig. 4.16 and 4.17). Two regions of high temperature develop from the 15 GHz input frequency (Fig. 4.16) as opposed to the one region of high temperature that developed from the 6.8 GHz excitation (Fig. 4.11).

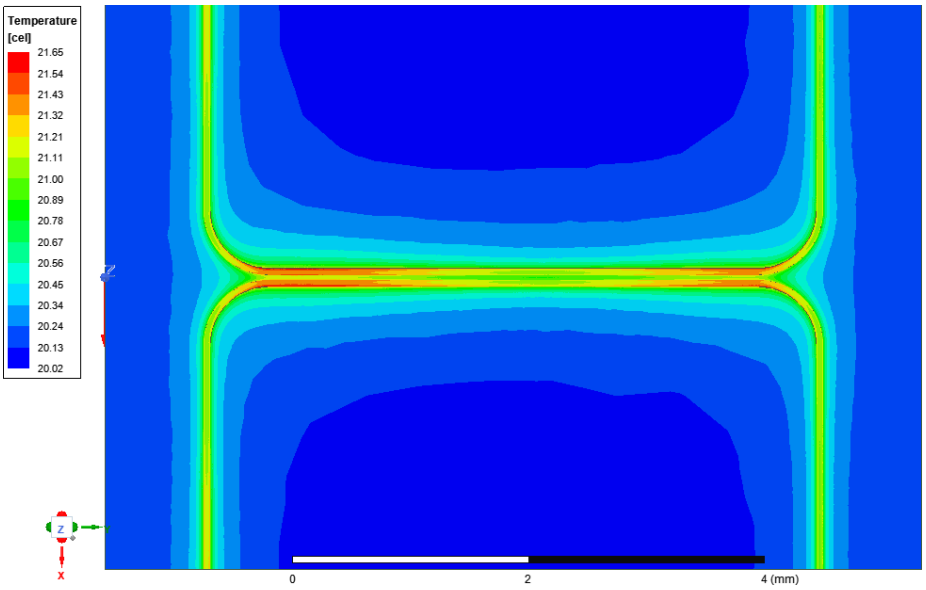

Figure 4.16: Temperature from parallel 15 GHz input signals ($\phi = 0°$) at top and bottom left ports plotted above two parallel microwave traces.

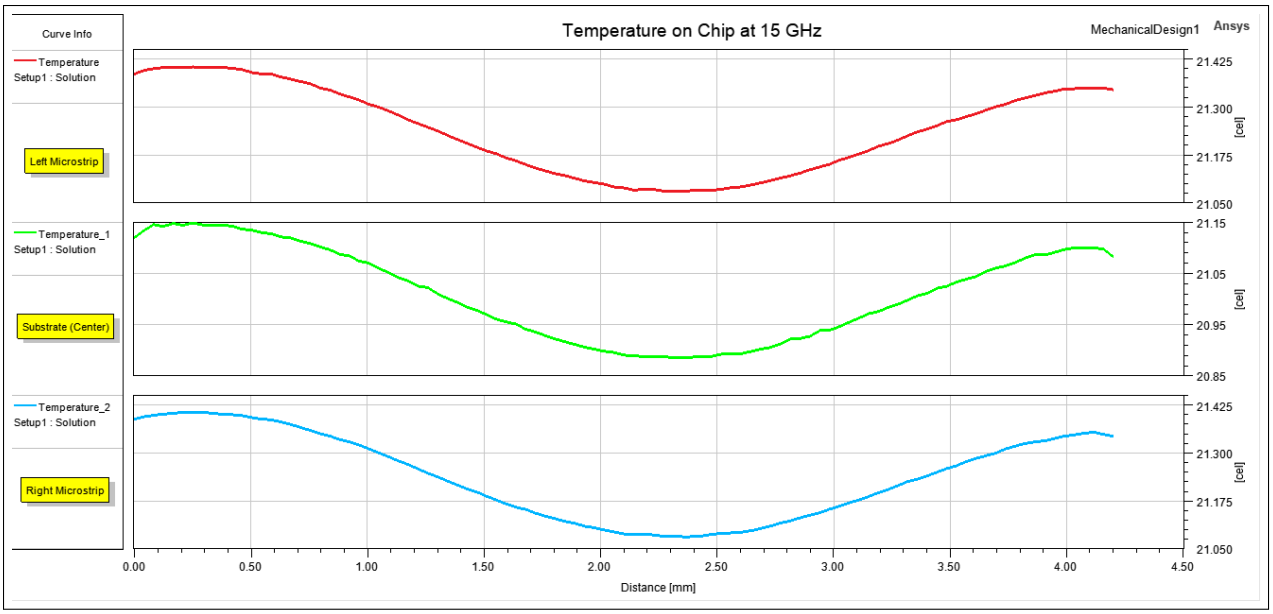

Figure 4.17: Temperature from parallel 15 GHz input signals ($\phi = 0°$) at top and bottom left ports plotted as functions of distance along length of both traces and center line. Total $\Delta T = 0.325°C$ for each microstrip.

The temperature plot resembles a smoothed-out, sinusoidal version of the current plot, which also showed two maximums. The temperature peaks at 21.4°C (Fig. 4.17).

4.2.3 Dual Trace Excitation ($\phi = 180$ °)

These simulations will be for the odd mode, in which currents run in opposite directions between traces.

6.8 GHz Inputs

The magnetic field and surface current density on the chip for odd mode propagation is solved for. Fig. 4.18 shows the magnetic field on a plane 5 µm above the chip surface.

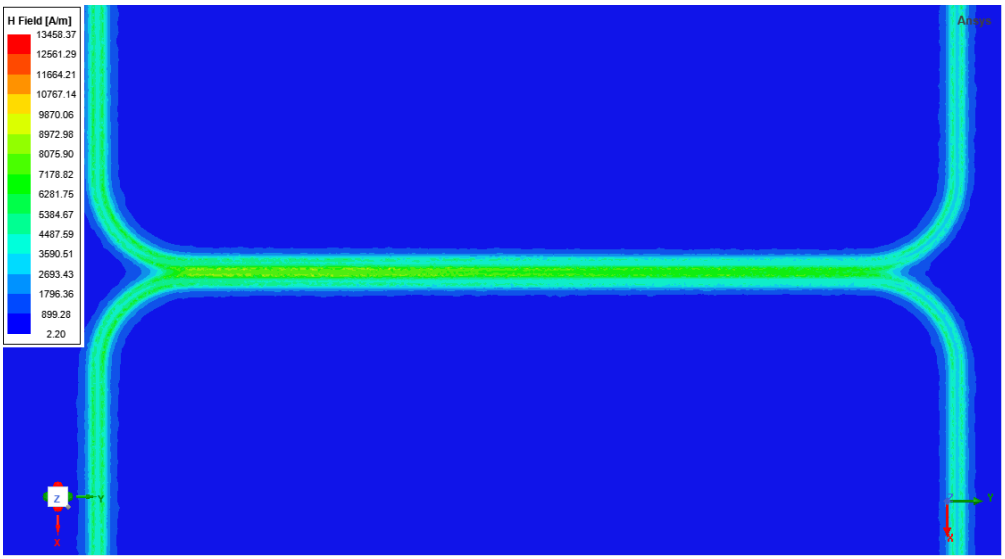

Figure 4.18: Magnetic field distribution from parallel 6.8 GHz input signals ($\phi = 180°$) at top and bottom left ports plotted above two parallel microwave traces.

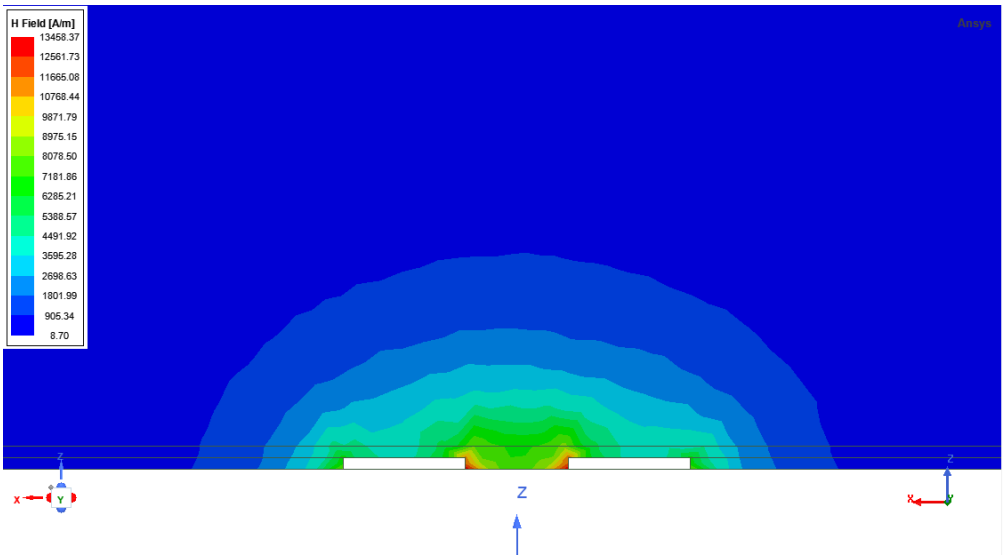

Figure 4.19: Magnetic field distribution from parallel 6.8 GHz input signals ($\phi = 180°$) plotted at central cross-section of two traces and substrate.

As shown in Fig. 4.18 and 4.19, the field distribution is highest in the area between traces due to the AC proximity effect. The area between traces is an area of high magnetic field, rather than a minimum.

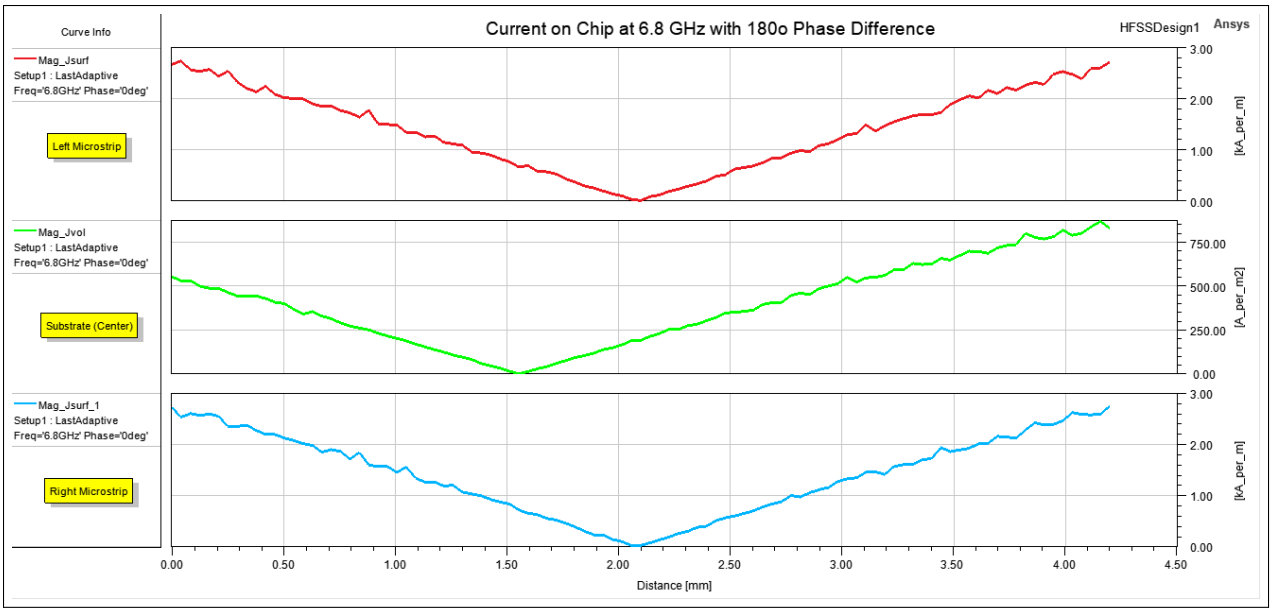

Figure 4.20: Magnitude of current density from parallel 6.8 GHz input signals ($\phi = 180°$) plotted as functions of distance along length of both traces and center line.

A shown in Fig. 4.20, the current plotted through the center of the traces takes a similar form as of that in the even mode configuration. The minimum (zero) current is at x = 2.08 mm.

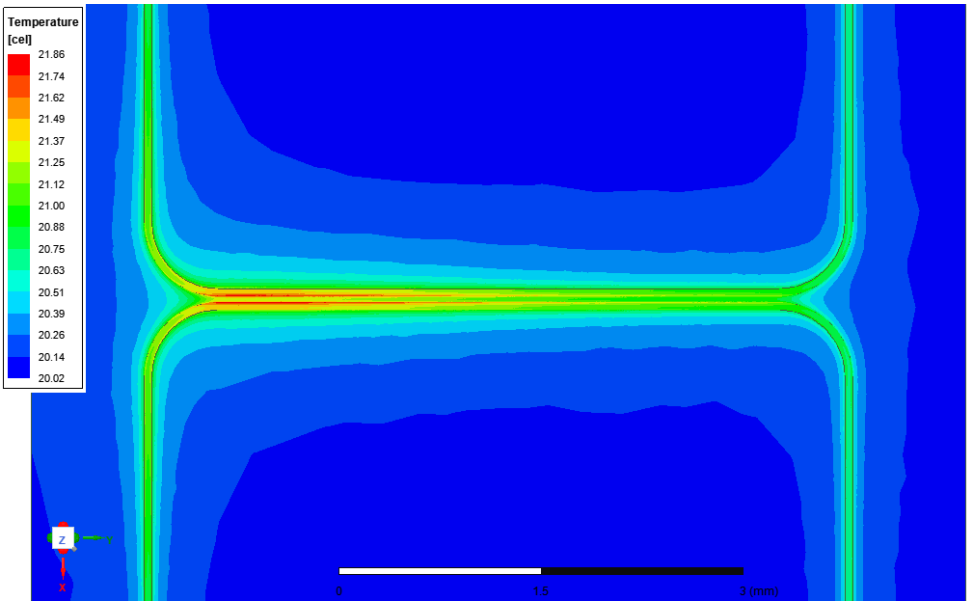

Figure 4.21: Temperature from parallel 6.8 GHz input signals ($\phi = 180°$) at top and bottom left ports plotted above two parallel microwave traces.

Notably, the temperature distribution in Fig 4.21 directly mirrors (i.e., looks the same flipped around a vertical line) the temperature distribution for 6.8 GHz excitation and even mode propagation (see Fig. 4.11 and 4.12). It is not clear why this occurs, but it is a behavior that arises from the symmetry/anti-symmetry of current direction in the traces.

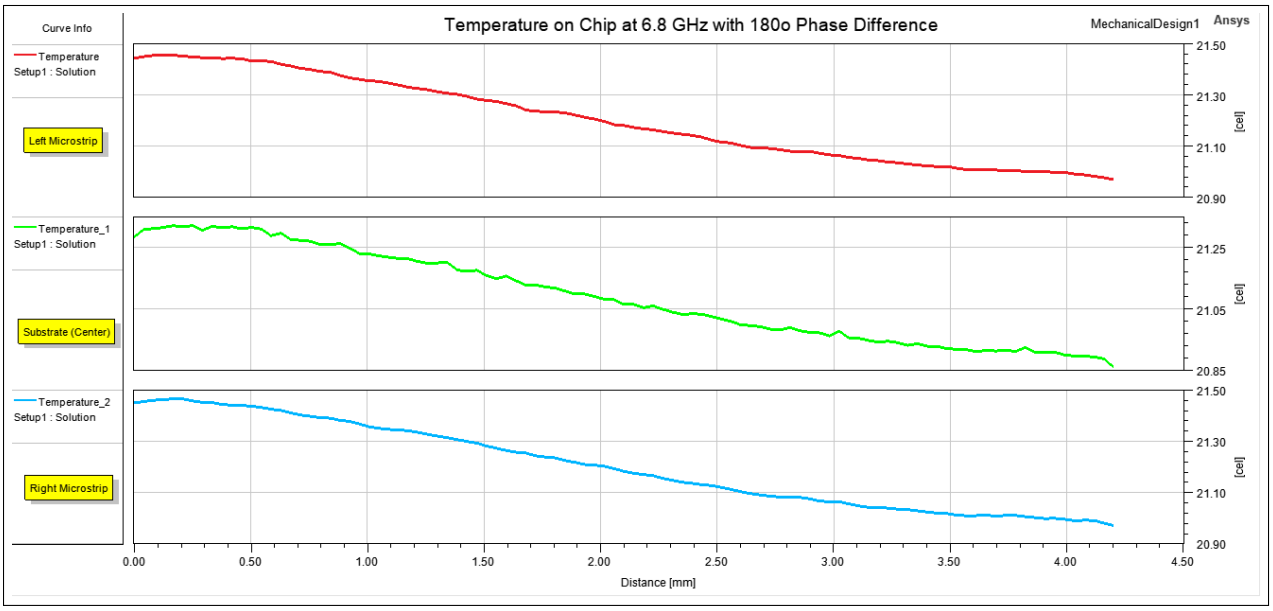

Figure 4.22: Temperature from parallel 6.8 GHz input signals ($\phi = 180°$) plotted as functions of distance along length of both traces and center line. Total $\Delta T = 0.50°C$ for each microstrip.

The maximum temperature on this model is 21.46°C (Fig. 4.22).

15 GHz Inputs

The magnetic field and surface current distribution for 4.2 mm long traces with 15 GHz inputs is shown in Fig. 4.23, Fig. 4.24, and Fig. 4.24.

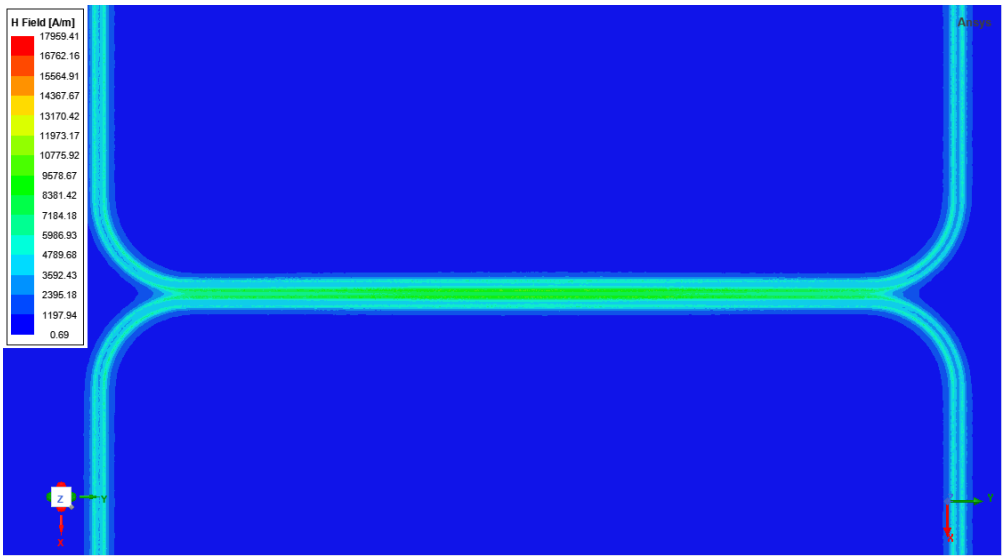

Figure 4.23: Magnetic field distribution from parallel 15 GHz input signals ($\phi = 180°$) at top and bottom left ports plotted above two parallel microwave traces.

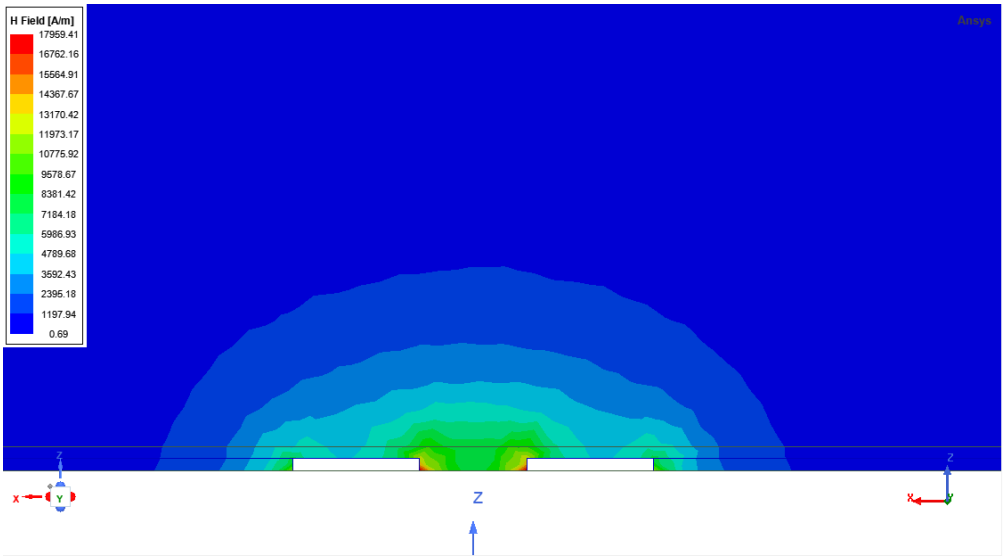

Figure 4.24: Magnetic field distribution from parallel 15 GHz input signals ($\phi = 180°$) plotted at central cross-section of two traces and substrate.

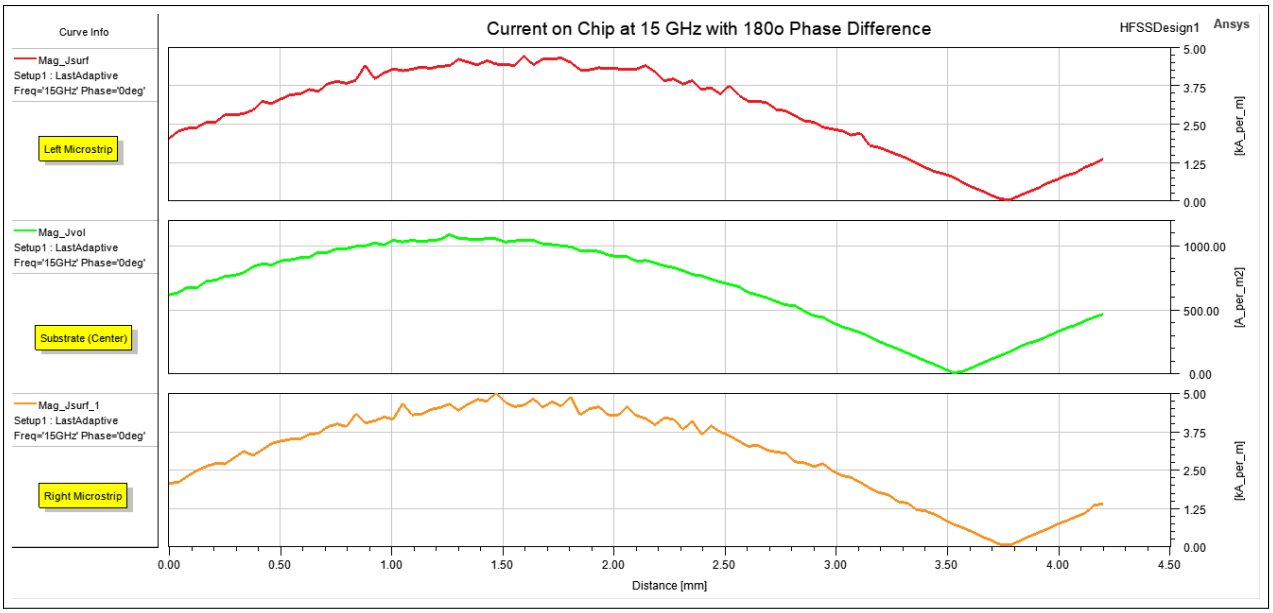

Figure 4.25: Magnitude of surface current density from parallel 15 GHz input signals ($\phi = 180°$) plotted as functions of distance along length of both traces and center line.

This longitudinal current behavior (Fig. 4.25) is qualitatively similar to the case of 15 GHz and ϕ=0° (see Fig. 4.15). The currrent now reaches its its minimum 0 further down the trace, at 3.75 mm.

The temperature distribution is shown in Fig. 4.26 and 4.27.

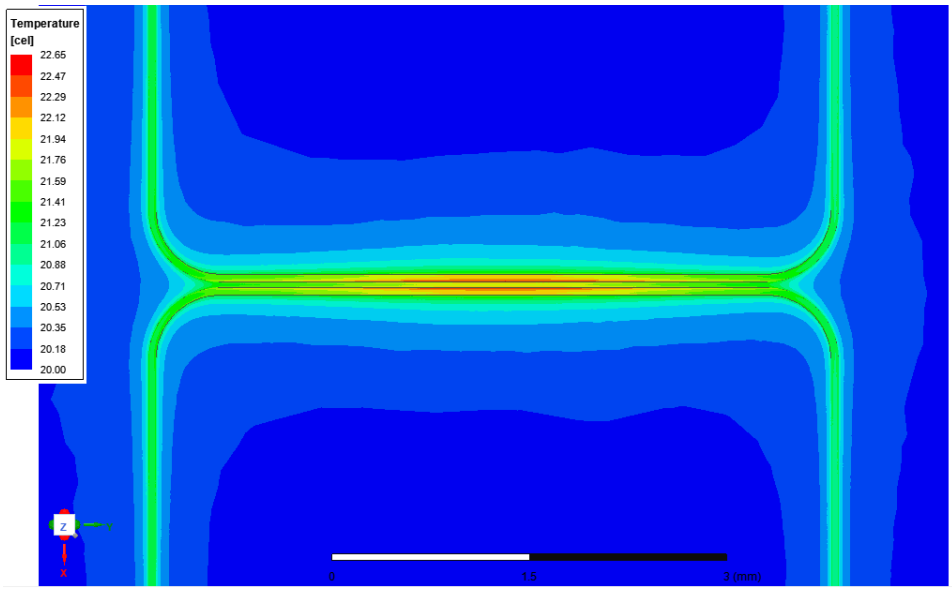

Figure 4.26: Temperature from parallel 15 GHz input signals ($\phi = 180°$) at top and bottom left ports plotted above two parallel microwave traces.

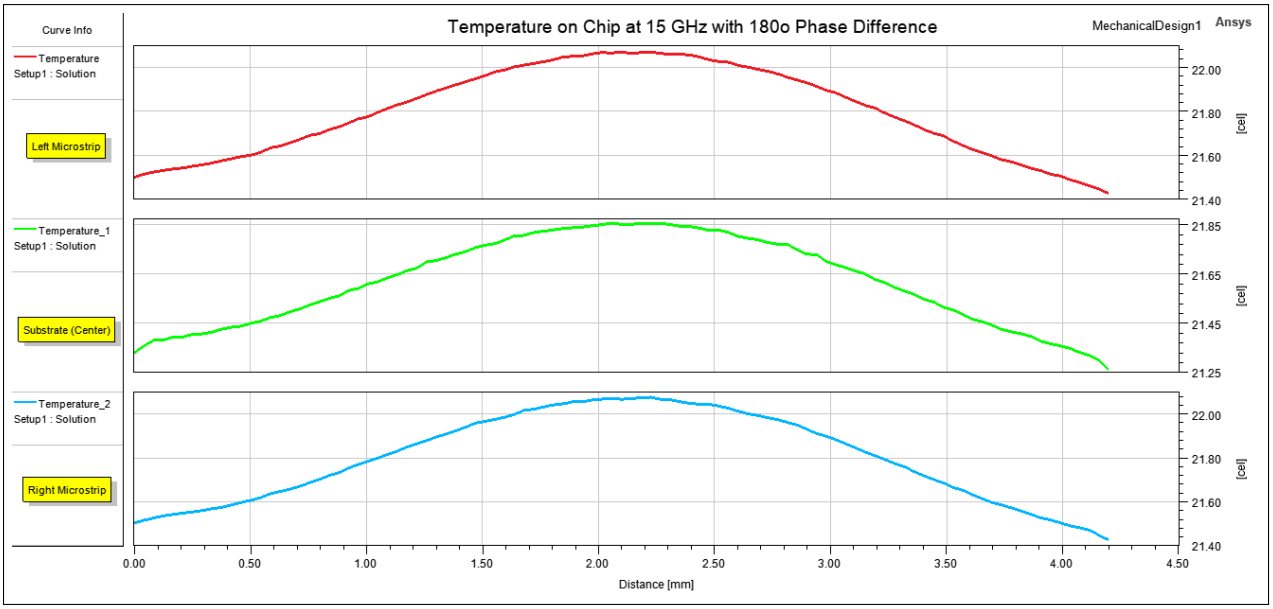

Figure 4.27: Temperature from parallel 15 GHz input signals ($\phi = 180°$) plotted as functions of distance along length of both traces and center line. Total $\Delta T = 0.68°C$ for each microstrip.

For this particular setup, the model reaches its peak temperature at 2.25mm, around halfway down the trace. Its peak temperature is 22.1 °C (Fig. 4.27).

4.3 Large Scale Two-Trace Model

The 24mm long trace model is tested with an excitation on a single port, with all other ports having 50 Ω terminations.

4.3.1 15 GHz

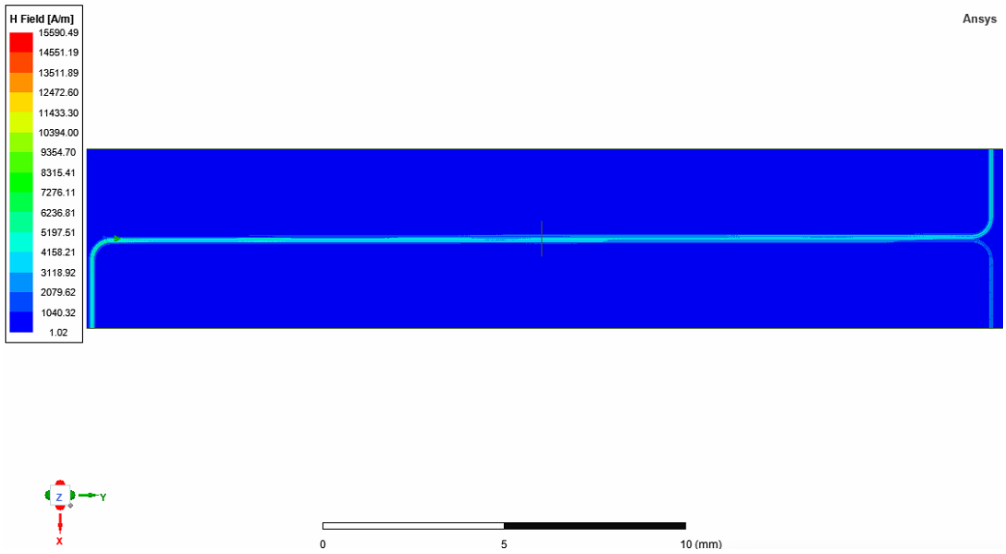

Figure 4.28: Magnetic field distribution from single 15 GHz input signal at bottom left port plotted above two parallel 24 mm microwave traces.

For the long traces, most of the field seems to "hop over" to the neighboring trace (Fig. 4.28). It is also visible, although difficult to see, that there is back-and-forth transfer of the magnetic field concentration.

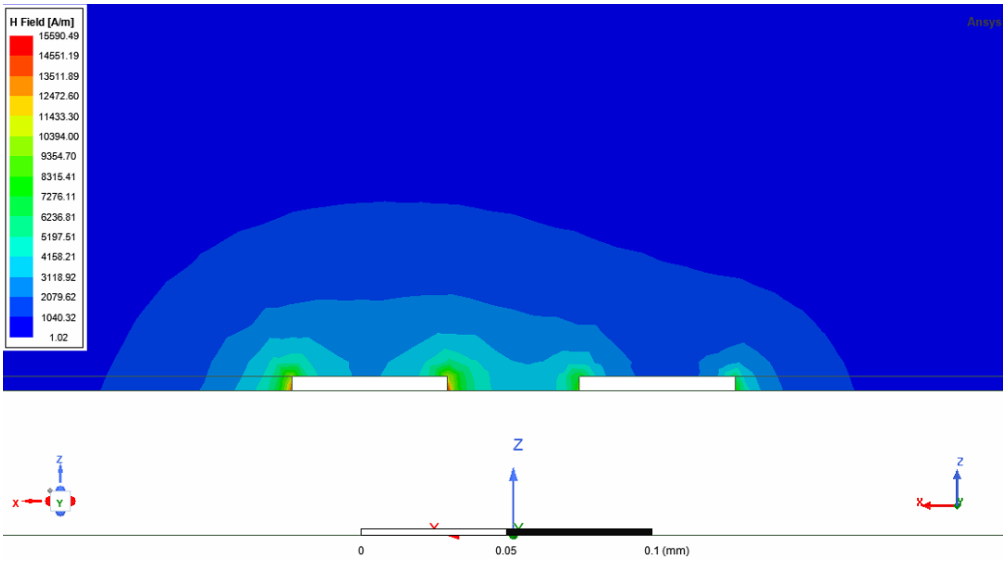

Figure 4.29: Magnetic field distribution from single 15 GHz input signal plotted at central cross-section of two 24 mm traces and substrate.

In Fig. 4.29, we can see that the minimum in the magnetic field is actually above the lower (right) input trace, since most of the microwave power has migrated over to he upper (left) trace.

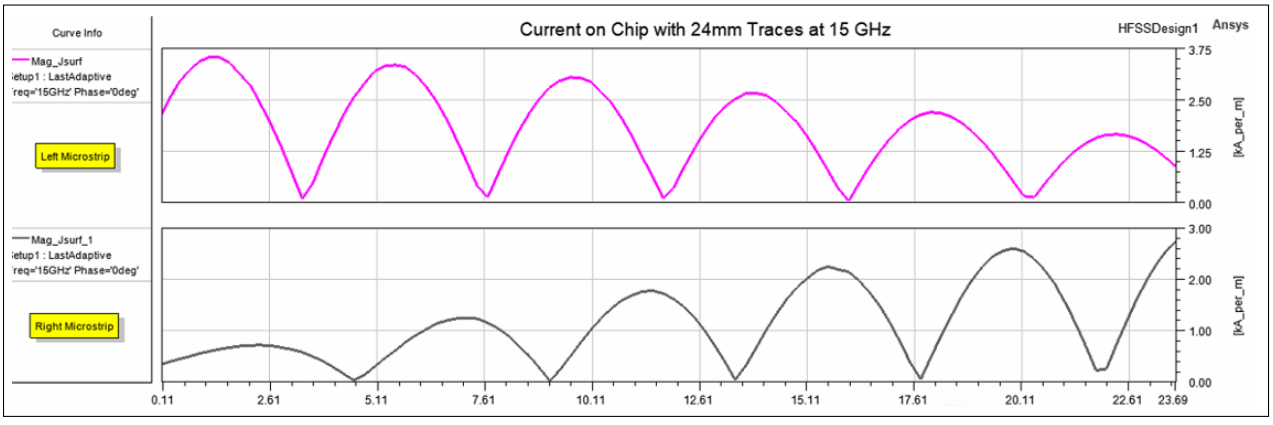

Figure 4.30: Magnitude of surface current density from single 15 GHz input signal plotted as functions of distance along length of both traces.

As shown in Fig. 4.30, power transfer between the traces can be observed in the periodic

structure of the plotted current. The peaks on the left microstrip more-or-less align with the troughs in the right microstrip, although not perfectly. The left microstrip's current gradually decreases in total amplitude, while the right microstrip's gradually increases. This matches the behavior seen in the plotted magnetic field, where most of the field concentration seems to transfer to the right/top trace.

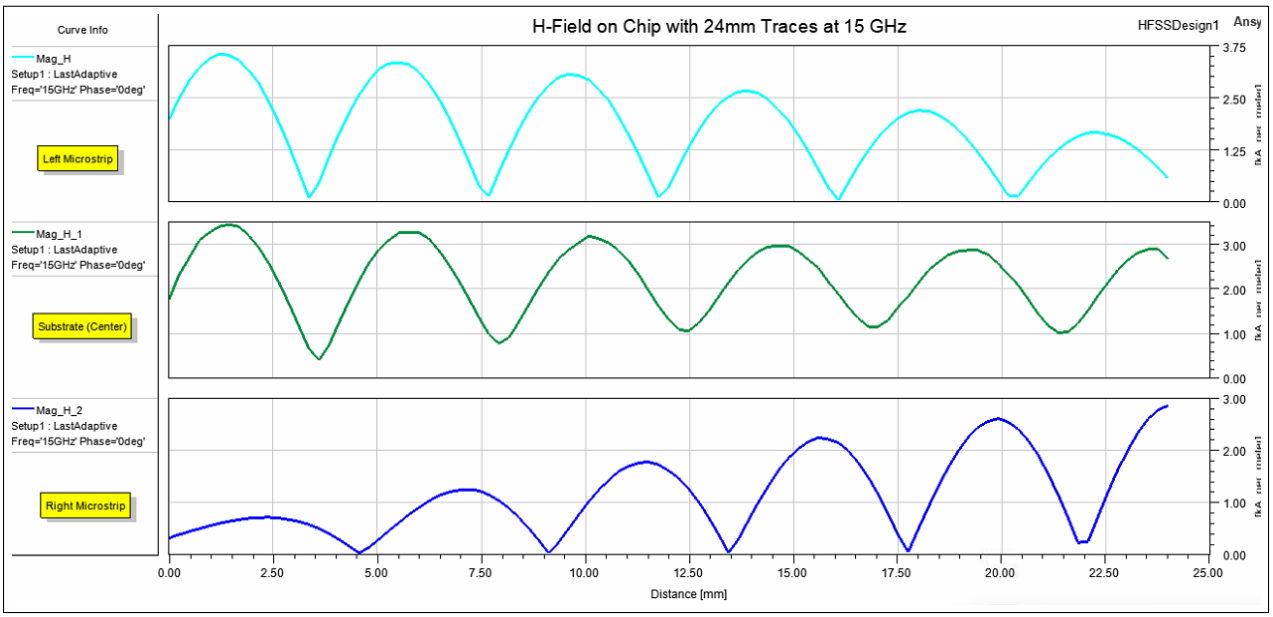

Figure 4.31: Magnitude of magnetic field from single 15 GHz input signal plotted as functions of distance along length of both traces and center line.

As the periodic behavior was of special interest in this model, the magnetic field along the distance on the trace was also plotted (Fig. 4.31). The magnetic field on the left and right microstrips follows the same structure as the current plot. Here, it is also visible that a section of the propagating wave solution is present in the substrate, between traces.

4.3.2 30 GHz

In an effort to accentuate the transfer of microwave power between the two traces, the same simulation was run at 30 GHz (see Fig. 4.32).

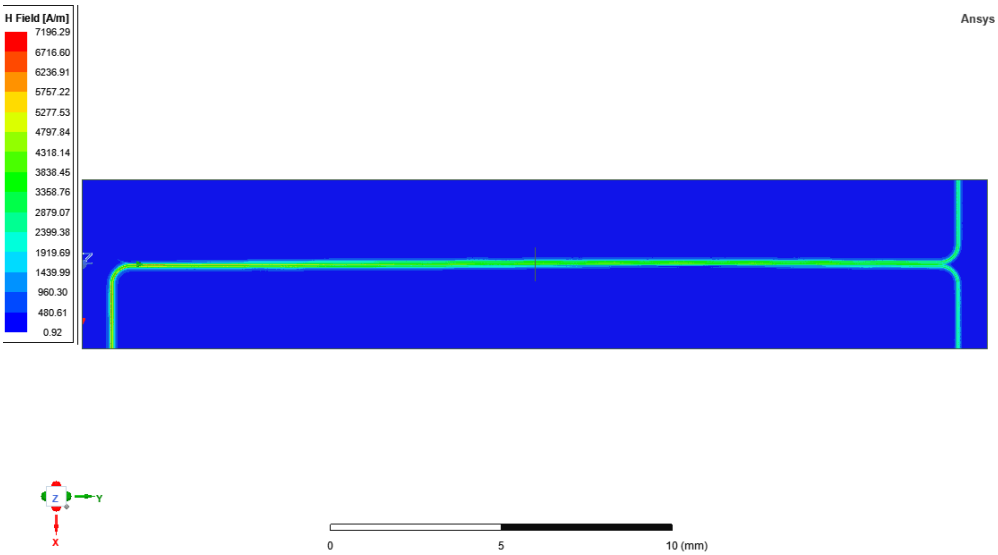

Figure 4.32: Magnetic field from single 30 GHz input signal at bottom left port plotted above two parallel 24 mm microwave traces.

In this simulation, the magnetic field distribution starts concentrated in the driven trace, periodically moves back-and-forth between traces, and in the end, splits off evenly between the two traces. Fig. 4.33 shows the magnetic field distribution at the midpoint along the traces.

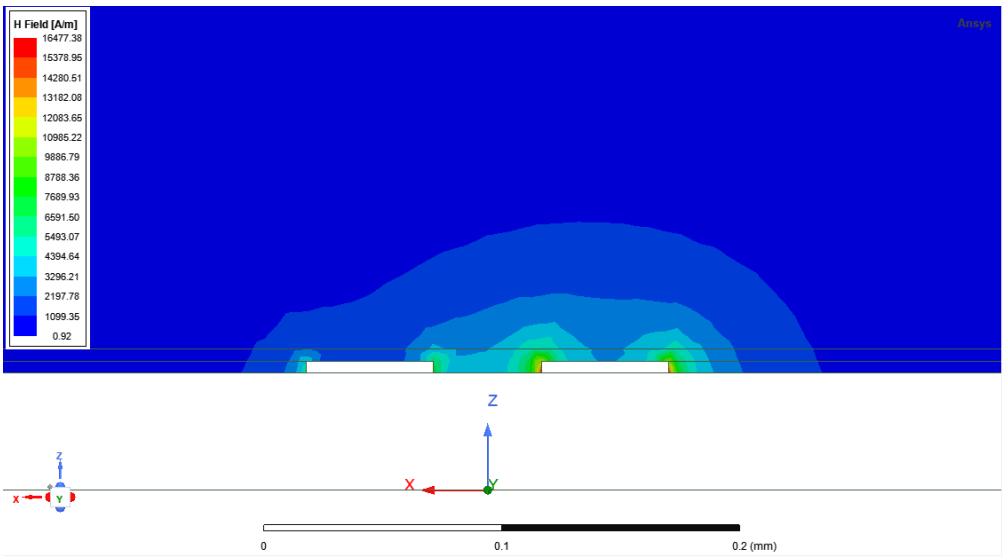

Figure 4.33: Magnetic field from single 30 GHz input signal plotted at central cross-section of two 24 mm traces and substrate.

With a 30 GHz excitation, the magnetic field in the middle of the device has its minimum above the left trace. It appears like a mirrored image of the magnetic field at this cross-section plane with 15 GHz excitation.

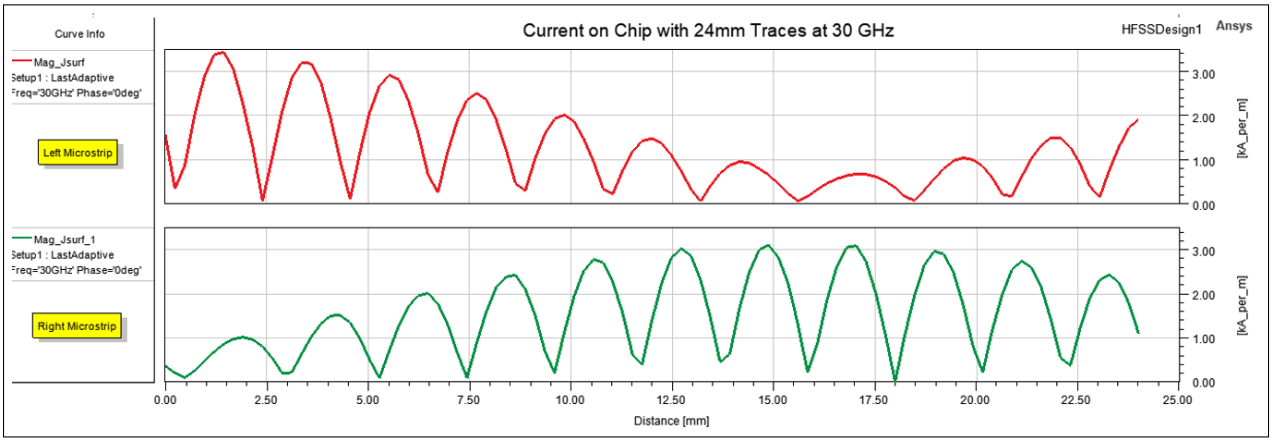

Figure 4.34: Magnitude of surface current density from single 30 GHz input signal plotted as functions of distance along length of both traces.

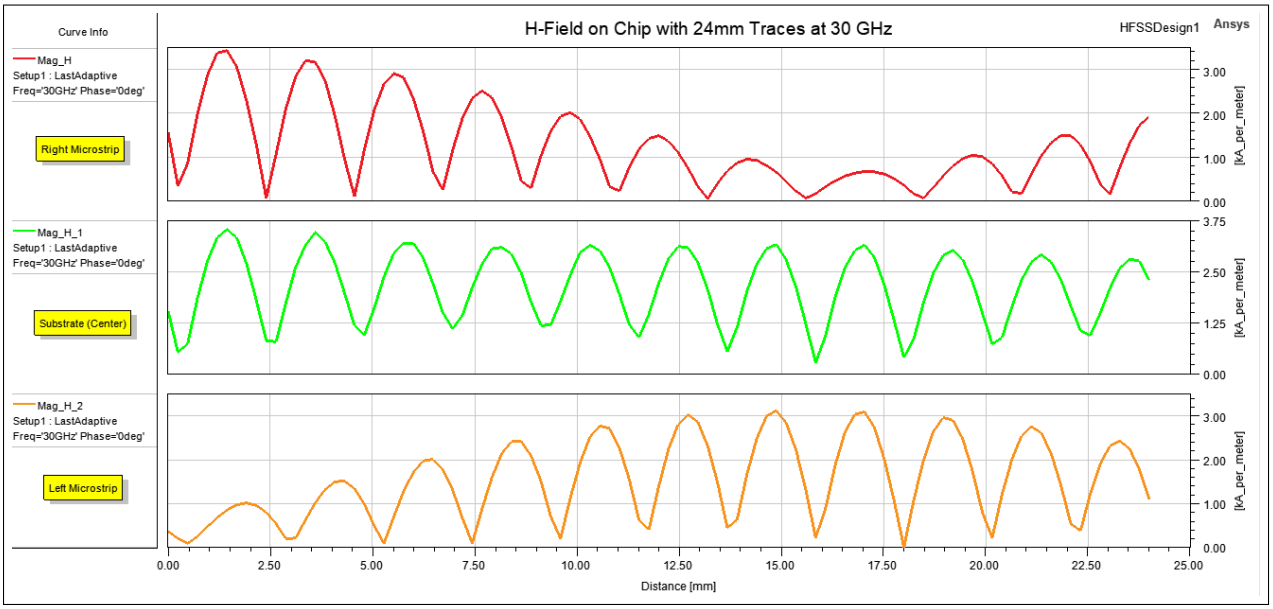

Figure 4.35: Magnitude of magnetic field from single 30 GHz input signal plotted as functions of distance along length of both traces and center line.

Periodic power transfer between the traces can be observed in the periodic structure of the plotted current and magnetic field (see Fig. 4.32 and 4.35, respectively). However, peaks

on the left microstrip don't quite align with the troughs in the right microstrip. Further, at a distance of around 17.5 mm, there is a switch, and the left microstrip's amplitude starts increasing while the right microstrip's amplitude starts decreasing.

Chapter 5

Discussion

5.1 Results Overview and Comparison to Theory

5.1.1 Single Trace Model

In the simulations of the single trace model, it was observed that magnetic field and current are stronger and more concentrated along the edges of the trace. It was also observed that the current prefers the inner edge of curves.

Another significant observation was the current and field dissipate along the trace (Fig. 4.5). Copper, which has a finite conductivity, is used in this model. The current is likely decaying due to resistive losses. The surface current induces Joule heating, and power decays along the path of propagation (Fig. 4.4). The magnetic field also visibly decays along the trace (Fig. 4.3). Electromagnetic energy is likely leaking into the dielectric as heat. This affects both the field and the current distribution.

Another possible source of power loss is mode mismatch. Curves may excite higher-order

modes, while the wave ports used in this simulation can only inject or receive one dominant mode. This mode mismatch could potentially cause power loss. This effect could be lessened by allowing more modes at each port, which can be done in HFSS. More investigation is needed to determine whether this is a significant source of power loss.

At 15GHz, high-frequency effects come into play. We see the current along the trace decrease, reach zero, and then increase again in Figure 4.5. This is assumed to be an effect from a standing wave pattern. With a shorter wavelength, the electrical length of the curved trace is larger in relation. The electrical length here can be defined as [21]:

$$\text{Electrical Length} = \frac{l}{\lambda} = \frac{\text{Physical length}}{\text{Wavelength}} \tag{5.1}$$

So, at higher frequencies, reflections from the curve and ports are more strongly felt. The bends and ports are both sources of reflection. The curve acts as an impedance discontinuity or perturbation. Then, at 15 GHz, a standing wave pattern is formed, causing the current magnitude to increase again after hitting 0. At 6.8 GHz, the wavelength is longer, so the physical structure causing the discontinuity is less "visible" to the wave, resulting in weaker reflections than in the higher frequency case.

5.1.2 4 mm Two-Trace Model

Single Excitation

In both the field and current plots, the field distribution and current, respectively, migrate to the inactive trace. The jump can be explained by inductive coupling and capacitive coupling. Changing current produces magnetic flux between the two conductive traces, which in turn induces current on the passive trace. In capacitive coupling, voltage change on the driven trace induces a displacement current in the non-driven trace. Inductive coupling

is driven by the magnetic field, while capacitive coupling is driven by the electric field.

Dual Excitation

For even mode propagation, the field concentrates most strongly on the outer edge of each transmission line (Fig. 4.8, 4.9, 4.13, and 4.14). When parallel currents flow, the field overlap between the two traces makes it appear as if it were a single, bigger trace (Fig. 4.8 and 4.13). The current magnitude reaches 0 at some point along the trace and then begins to increase again (Fig. 4.5). This can be seen in all current plots, forming a wave-like pattern from the change in phase orientation in the current density as it moves along the trace. It can be noted that the current minimum at the microstrips does not exactly match the location of the minimum of the current in the dielectric substrate, which reaches its minimum further down the trace for even mode (see Fig 4.10 and 4.15) and earlier along the trace for odd mode (see Fig. 4.20 and 4.25).

Displacement current is a measure of how the electric field leaks into the substrate, and is given by the partial derivative of $\mathbf{E}$ in the Maxwell-Ampere law:

$$\nabla \times \mathbf{B} = \mu_0 \mathbf{J} + \mu_0 \epsilon_0 \frac{\partial \mathbf{E}}{\partial t}, \tag{5.2}$$

where $\mathbf{J}$ is the relevant current density. The displacement current's minimum being further downstream along the traces than the surface current minima shows that the electric field in the dielectric is out of phase with the currents.

At the higher frequency of 15 GHz, the current plot begins to look like a smooth curve (see Fig. 4.15 and 4.25). This is an effect of stronger coupling, wherein the current is no longer just effected by interference, but is beginning to fall into a continuous back-and-forth periodic redistribution of energy along the curves. This effect is further explored in the 24 mm trace model.

The cross-section of the middle of the atom chip (Fig. 4.14 and 4.19) shows that with phase difference $\phi = 0°$ (even mode), fields around the trace effectively destructively interfere in the space between, creating a magnetic field minimum there (Fig. 4.14). When $\phi = 180°$ (odd mode), the opposite occurs, and the field is strongest in the middle. The area of high field draws currents and charges towards it, causing current to hug the outer edge in even mode and the inner edge in odd mode (Fig. 4.19).

For this dual excitation, two-trace model, thermal simulations were run.

For the thermal simulations, the impact of additional heating from phase and frequency variation was of interest. The maximum temperature values were as follows:

Table 5.1: Maximum Temperature and Total Temperature Change Along Microwave Traces with Different Frequencies and Phase Differences

Frequency (GHz)	**Phase ϕ (°)**	**Max Temperature (°C)**	**ΔT (°C)**
6.8	0	20.95	0.20
6.8	180	21.46	0.50
15	0	21.40	0.325
15	180	22.10	0.68

15 GHz excitation induces additional heating, as does the odd mode. The current hugging the inner edges of the traces in odd mode causes electric field and charge to concentrate in a smaller region, which induces additional heating.

5.1.3 24 mm Two-Trace Model

In this simulation (Fig. 4.28-35), the field and current hopping between traces that could be seen in the smaller model (under single excitation) is further explored. The model is

elongated and frequency is increased, so that the field and current has room to hop back and forth between the traces. This power oscillation is somewhat similar to a microwave lattice. A standard microwave lattice is formed by two counter-propagating microwave fields.

In order to understand how waves propagate in this trace, we revisit equation (2.1):

$$I(z) = A_{even}e^{-\gamma z} + A_{odd}e^{\gamma z},$$

Since $\gamma = \alpha + i\beta$, this can be written as [12]

$$I(z) = A_{even}e^{-i\beta z} - A_{odd}e^{i\beta z} \tag{5.3}$$

for the phase constant (the imaginary part of the propagation constant) β, which is defined by the wavelength as:

$$\lambda = \frac{2\pi}{\beta}$$

The driven trace supports both even and odd modes, represented by the $e^{-i\beta z}$ and $e^{i\beta z}$ terms propagating in the +z and -z directions, respectively. Since $\beta_{\text{even}} \neq \beta_{\text{odd}}$, the modes fall more and more out of phase from each other as they propagate. Power oscillation between the traces arises from this superposition of even and odd propagation modes with different propagation constants, β. As the relative phase difference accumulates with distance along the trace, periodic constructive and destructive interference occurs on the conductive traces. This results in the hopping back-and-forth behavior seen in section 4.3.

Equation (5.3) expresses a wave consisting of two oppositely propagating components along a microwave trace. When these components interfere, the amplitude becomes [22]:

$$|I(z)|^2 = |A_{\text{even}}|^2 + |A_{\text{odd}}|^2 - 2|A_{\text{even}}||A_{\text{odd}}|\cos(2\beta z + \Delta\phi) \tag{5.4}$$

where the cosine term represents the slow-moving envelope produced by interference between

waves. $\Delta\phi$ here is the time-dependent phase difference between waves. This slow-moving envelope is somewhat visible in Fig. 4.35.

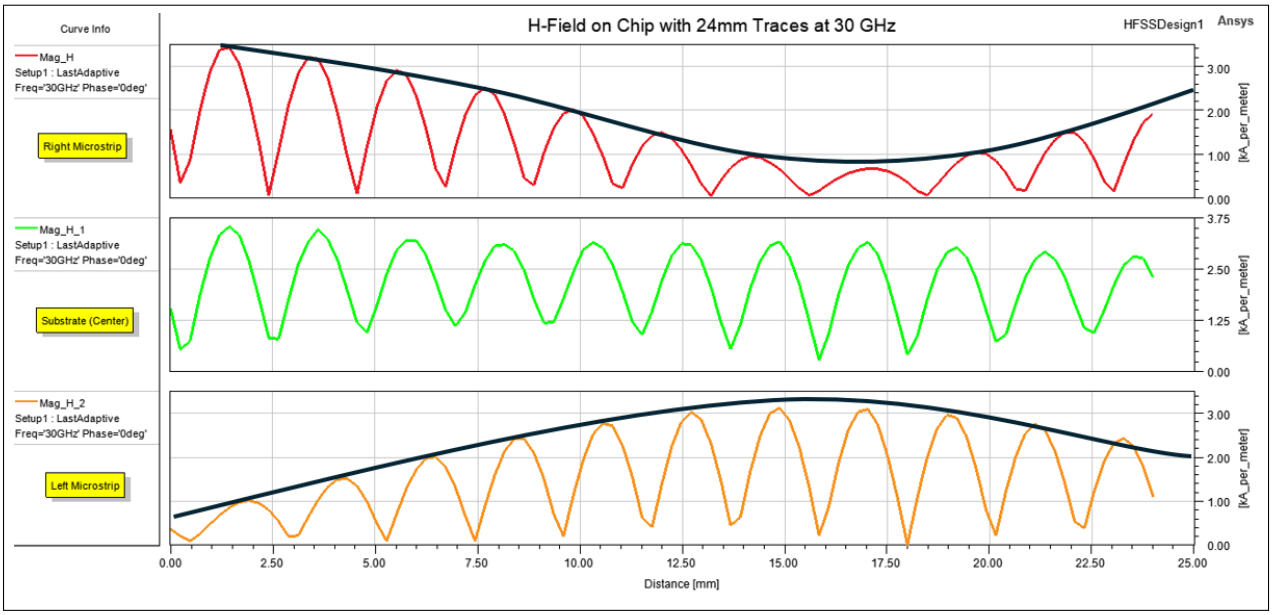

Figure 5.1: Magnitude of magnetic field from single 30 GHz input signal plotted as functions of distance along length of both traces and center line, with slow-moving envelope wave shown as black lines. Figure adjusted from Fig. 4.35.

Periodic power transfer between the traces can be observed in the periodic structure of the plotted current (Fig. 4.30 and 4.31). Ideally, the peaks on the left microstrip would align perfectly with the troughs in the right microstrip. This would indicate perfect lossless coupling. Unfortunately, this was not the case. It is likely that mode mismatches and reflections from the bends and ports slightly distorted the system.

In the 15 GHz excitation simulation, the outputs are strongly asymmetrical. The left microstrip's current gradually decreases in total amplitude, while the right microstrip's gradually increases (Fig. 4.30). This matches the behavior seen in the plotted magnetic field, where the magnetic field distribution overwhelmingly hops over to the non-driven trace (Fig. 4.28). This is generally due to a multiple of the coupling length (distance needed for the even/odd mode phase difference completely exchange power) being close to the device length.

At 30 GHz, the outputs are much more symmetric. The field distribution splits relatively evenly between the two traces (Fig. 4.32). the magnetic field distribution starts concentrated in the driven trace, periodically moves back-and-forth between traces, and in the end, splits off evenly between the two traces. Oscillations are more rapid and the power appears more even between the two traces. The transfer happens so fast that it does not end up appearing as asymmetry, like in the 15 GHz case.

In the 30 GHz excitation model, periodic power transfer between the traces can be observed in the periodic structure of the plotted current and magnetic field (Fig. 4.34). However, peaks on the left microstrip don't quite align with the troughs in the right microstrip, as is needed for an ideal microwave lattice. Further, at a distance of around 17.5 mm, there is a switch, and the left microstrip's amplitude starts increasing while the right microstrip's amplitude starts decreasing. This is where the field distribution symmetrically distributes itself between the two transmission lines.

5.2 Interpretation

The simulations completed provide valuable information regarding wave behavior along traces, particularly for a microwave atom chip using this particular geometry of curved traces. Frequencies previously unused were tested, thermal effects were evaluated, and an alternate, longer design was explored for the potential of generating a microwave lattice structure. All of the information gathered over the course of these studies helps to inform potential limitations of the atom chip (reflections, impedance and mode mismatches, heating), as well as possibilities for new uses (microwave lattice).

5.3 Solver Performance and Potential Error

In terms of errors present in the implementation of numerical solver, possible sources uncertainty are the mesh convergence, solution convergence, frequency sweep, and wave port accuracy. I used a Maximum Delta S parameter of 0.005 for smaller models and 0.01 for larger models, with 99 adaptive passes. My solutions all converged, so this should not be an error source. The meshing, however, can always be made finer. Unfortunately, this is limited by the capabilities of the computer running the program. By Ansys's specifications, my Delta S parameter should have been more than sufficient. The frequency sweep, I believe, is a more likely source of uncertainty and potentially error. I used an interpolating sweep of 0-20 GHz for smaller models, and an interpolating sweep of 14-16 GHz and 29-31 GHz (respectively for 15 GHz and 30 GHz excitation) for the large models. Interpolation tends to smooth out features, which can distort sharper coupling features, particular in the case of the microwave lattice. The wave port can be a source of uncertainty if it is sized incorrectly (which the one used in these simulations, by Ansys specifications, is not) or from mode purity errors and impedance mismatches upon excitation. The restriction to single mode set on the wave ports may have caused mismatches and asymmetries in my model.

5.4 Design Iterations

The designs simulated in this thesis were iterated as follows. First, a single trace was created, in order to observe the basic behavior of a realistic atom chip simulation. It was noted that there was noticeable power dissipation along the trace. Then, another trace was added to "pick up" this dissipated power. From here, a longer model was created to test whether the power that transferred to the adjacent (to the driven) trace would hop back to the driven trace. Once it was confirmed that this could happen, the simulation was driven at

higher frequencies to maximize this effect and construct a microwave lattice-like structure.

The smaller two-trace model was used to test features of dual excitation and even vs odd modes. When the tendency of current to accumulate at the edges of the trace was noted, a thermal simulation was added to see whether this would result in excessive heating.

5.5 Limitations

The major limitations of this model are also features of the model. The intent of this work is to produce models of a real microwave atom chip that might be used in a research lab. However, an ideal coupled system requires a long transmission line to see well-defined hopping back-and-forth behavior. The longest model simulated was only 24 mm. A 72 mm trace simulation was attempted, but turned out to be too intensive for the computer to complete. The use of copper and air, instead of a perfect electric conductor and vacuum, also contribute to additional power loss and distortions that would be present in the real-world, but are unideal for simulating physical concepts.

The wave port excitation used is another limitation, as it is difficult to identify whether there are higher-order modes present. In creating the wave port, the mode is already assigned, which could end up being disruptive. 1 mode was allowed, which is usually appropriate for a microstrip, but 2 or more is better practice for fully capturing even/odd mode propogation [13]. Another feature of HFSS that may have been limiting is the meshing. A network of interconnected volumes can never fully capture real-world behavior.

The final significant limitation is that in plotting the currents in fields, I used either a 1-dimensional line or 2-dimensional planes to extract quantities from a 3-dimensional field. This may have left artifacts in my data and failed to fully capture energy distributions.

Chapter 6

Conclusion and Future Work

6.1 Contributions

I created a series of microwave atom chip models in Ansys HFSS capable of generating solutions to various types of simulations (electromagnetic or thermal) for various excitations (6.8 GHz, 15 GHz, or 30 GHz with $\phi = 0°$ or $\phi = 180°$). Each model is ready to be run with any combination of these excitations one may want to use and produce information on potential near field minima, current distributions, and wave propagation.

6.2 Evaluation of Objectives

In section 1.3, I outlined the project objectives as:

1. Design and build a microwave atom chip model in Ansys HFSS. ✓
2. Run electromagnetic simulations to verify that the model demonstrates intended be-

havior. ✓

3. Run thermal simulations to measure expected heating on the chip. ✓
4. Adjust the model geometry to optimize chip performance and study behavior-of-interest. ✓
5. Compare electromagnetic response of traces under various modes of excitation. ✓
    - Single-trace excitation. ✓
    - Dual-trace excitation with varied phase differences. ✓
6. Demonstrate a microwave lattice. ✓

Significant progress was made towards completing all of these objectives, but there is more work that could be done. In the case of the microwave lattice, I would consider the behavior I achieved lattice-like, rather than a complete, physically robust microwave lattice. There is still work to be done to generate better defined nodes. In the case of objective 6, I would have liked to try excitations with a greater variety of phase differences. In this work, I only tested the even and odd modes. In reality, there is a range of "in-between" phases that could yield interesting behavior.

Overall, a microwave atom chip model was designed and built and electromagnetic and thermal simulations were successfully run and used to evaluate the results of single-trace and dual-trace excitations with various phase differences. An adjusted, elongated model was used to generate microwave lattice-like behavior.

6.3 Broader Impact

This work used a realistic microwave atom chip model to explore the impacts of different excitation frequencies, different modes of operation (even/odd), and alternate geometries toward generating a microwave lattice. These models provide a platform on which any researcher working with a microwave atom chip can test design and implementation ideas. The solutions to these simulations can help predict where a trapped atom will be and how it might behave under certain conditions and excitations.

6.4 Future Work

In the future, it would be prudent to run these simulations under the following conditions:

1. Multiple (2-3) allowed modes at wave ports.
2. Perfect electrical conductor ground plane and traces with vacuum radiation boundaries.
3. Tighter frequency sweep (single point discrete sweep).
4. Phase differences of $\phi = 30°$, $\phi = 60°$, $\phi = 90°$, and $\phi = 270°$.
5. Infinite geometrical boundary conditions to model infinite traces.

In addition, it would be extremely beneficial to test the excitation conditions used in the simulations outlined here on a real microwave atom chip or prototype, and compare real-world results with simulation.

Bibliography

[1] Miyahira, W., Rotunno, A. P., Du, S., & Aubin, S. (2021) Microwave atom chip design. *MDPI Atoms,* 9(54). https://doi.org/10.3390/atoms9030054

[2] Cronin, A. D., Schmiedmayer, J., & Pritchard, D. E. (2009). Optics and interferometry with atoms and molecules. *Reviews of Modern Physics,* 81(1051). https://doi.org/10.1103/RevModPhys.81.1051

[3] Phillips, W. D. & Metcalf, H. (1982). Laser Deceleration of an Atomic Beam. *Physical Review Letters,* 9(48). 10.1103/PhysRevLett.48.596

[4] Neuhauser, W., Hohenstatt, M., Toschek, P., & Dehmelt, H. (1978). Optical-Sideband Cooling of Visible Atom Cloud Confined in Parabolic Well. *Physical Review Letters,* 4(41). 10.1103/PhysRevLett.41.233

[5] Anderson, M. H., Ensher, J.R., Cornell, E. A., Matthews, M. R., Wieman, C.E. (1995). Observation of Bose-Einstein Condensation in a Dilute Atomic Vapor. *Science,* 269(5221). 10.1126/science.269.5221.198

[6] Böhl, P., Riedel, M. F., Hoffrogge, J., Reichel, J., Hansch, W., & Treutlein, P. (2009). Coherent manipulation of Bose-Einstein condensates with state-dependent microwave potentials on an atom chip. *Nature Physics,* 5. https://doi.org/10.1038/nphys1329

[7] Agosta, C. C., Silvera, I. F., Stoof, H. T. C., & Verhaar, B. J. (1989). Trapping of Neutral Atoms with Resonant Microwave Radiations. *Physical Review Letters,* 62(60). 10.1103/PhysRevLett.62.2361

[8] Spreeuw, R. J. C., Gerz, C., Goldner, L. S., Phillips, W. D., Rolston, S. L., & Westbrook, C. I. (1994). Demonstration of neutral atom trapping with microwaves. *Physical Review Letters,* 72(20). https://doi.org/10.1103/PhysRevLett.72.3162

[9] S. Du, Ziltz, A. R., Miyahira, W., & Aubin, S. (2022). Suppression of potential roughness in atom-chip ac Zeeman traps, *Physical Review A,* 105 (053127). https://doi.org/10.1103/PhysRevA.105.053127

[10] Kruger, P., Andersson, L. M., Wildermuth, S., Hofferberth, S., Haller, E., Aigner, S., Groth., S, Bar-Joseph, I., & Schmiedmayer, J. (2007). Potential roughness near lithographically fabricated atom chips. *Physical Review A,* 76(063621). https://doi.org/10.1103/PhysRevA.76.063621

[11] Blackwell, A. E., Rotunno, A. P., & Aubin, S. (2020). Demonstration of the lateral AC skin effect using a pickup coil. *American Journal of Physics,* 88(8), pp. 676-683. https://doi.org/10.1119/10.0001272

[12] Pozar, D. M. (2011). *Microwave engineering* (4th ed.). John Wiley & Sons.

[13] Kopp, M. (2013). *An introduction to HFSS: Fundamental principles, concepts, and use.* Ansys Inc.

[14] EL Sabbagh, M. (2011) *Electromagnetic-Thermal Analysis Study Based on HFSS-ANSYS Link.* Electrical Engineering and Computer Science - Technical Reports. No. 46. https://surface.syr.edu/eecs_techreports/46.

[15] Army SBIR—STTR Program. *Aluminum Nitride-Based Monolithic Microwave Integrated Circuits.* U.S. Army SBIR—STTR. https://armysbir.army.mil/topics/

aluminum-nitride-monolithic-microwave-integrated-circuits/. Retrieved April 15th, 2026.

[16] Ansys, Inc. *S-Parameters.* Ansys Help. https://ansyshelp.ansys.com/public/Views/Secured/Electronics/v251/en/Subsystems/HFSS/Content/HFSS/SParameters.htm. Retrieved April 15th, 2026.

[17] Ansys, Inc. *Setting Maximum Delta S per Pass.* Ansys Help. https://ansyshelp.ansys.com/public/Views/Secured/Electronics/v251/en/Subsystems/HFSS/Content/HFSS/SettingtheMaximumDeltaSPerPass.htm. Retrieved April 15th, 2026.

[18] Ansys, Inc. *Maximum Delta S.* Ansys Help. https://ansyshelp.ansys.com/public/Views/Secured/Electronics/v242/en/Subsystems/HFSS/Content/HFSS/MaximumDeltaS.htm. Retrieved April 15th, 2026.

[19] Ansys, Inc. Calculating the PI impedance. Ansys Help. https://ansyshelp.ansys.com/public/Views/Secured/Electronics/v242/en/Subsystems/HFSS/Content/HFSS/CalculatingthePIImpedance.htm. Retrieved April 15th, 2026.

[20] Ansys, Inc. Calculating Net Power Flow through a Surface. Ansys Help. https://ansyshelp.ansys.com/public/Views/Secured/Electronics/v242/en/Subsystems/HFSS/Content/ReportsandPostProc/CalculatingNetPowerFlowthroughaSurface.htm. Retrieved April 15th, 2026.

[21] Drollinger, F. J. (1980). *Ground radio communications specialist (Vol. 7: Auxiliary circuits and systems)*, pp. 16–18. U.S. Air Force Technical Training School.

[22] Ellingson, S. W. (2018). *Electromagnetics, Vol. 1.* VT Publishing. https://doi.org/10.21061/electromagnetics-vol-1

Appendix A

Thermal Simulation of Microwave Atom Chip with Low Bulk Conductivity

The bulk conductivity of high grade bulk AlN is assumed to be 220 W/mK. However, it was found that this value decreases due to degradation of the material and impurities introduced during the manufacture process, as well as due to the particular thickness of AlN used in the chip. This lower bulk conductivity was determined to be 20 W/mK at the absolute lowest. Earlier exploratory simulations were done using a much thinner ground plane than that of the model used in this research. This thicker ground plane was eventually chosen because it yielded significantly less heating on the surface of the chip. The thin ground plane model is identical to the small scale atom chip model, but with a ground plane thickness of 5 µm (matching the thickness of the trace). A 6.8 GHz input at 20 W power was used in all simulations. These simulations were conducted in vacuum.

A.1 Thin ground plane

For a thin ground plane with 20 W/mK bulk conductivity in the substrate, it was found that change in phase difference from $\phi = 0°$ to $\phi = 180°$ increased the peak temperature on the chip significantly, from 20.7 to 25.1 degrees (shown in Fig. 1 and 2).

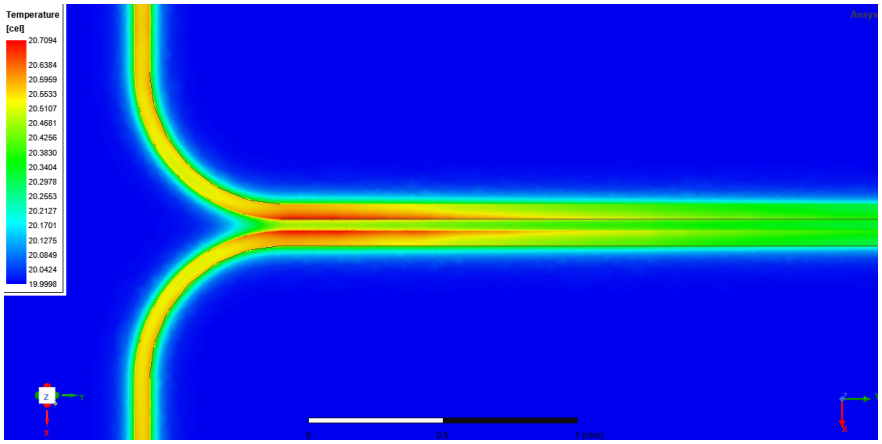

Figure 1: Thermal simulation of atom chip with thin ground plane, phase difference $\phi = 0°$, and 20 W/mK AlN bulk conductivity, showing peak temperature of approximately 20.7°C.

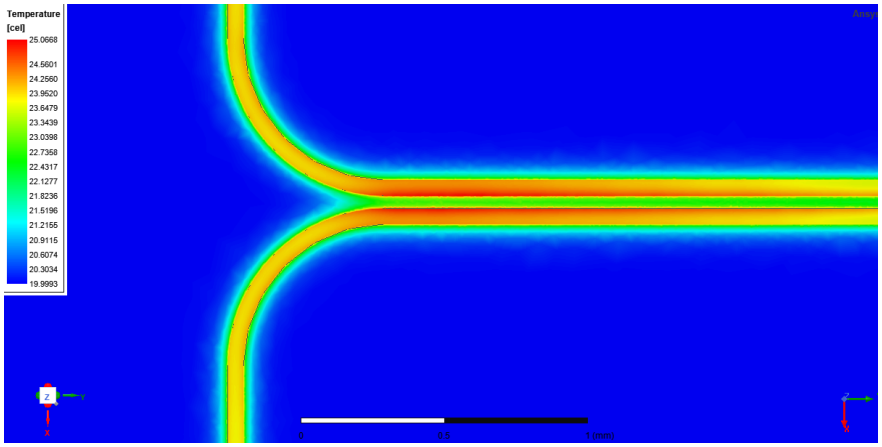

Figure 2: Thermal simulation of atom chip with thin ground plane, phase difference $\phi = 180°$ and 20 W/mK AlN bulk conductivity, showing peak temperature of approximately 25.1°C.

A.2 Thick ground plane

In the design with a thick ground plane, change in phase difference from $\phi = 0°$ to $\phi = 180°$ was found to yield a much smaller spike in temperature (Fig. 3 and 4).

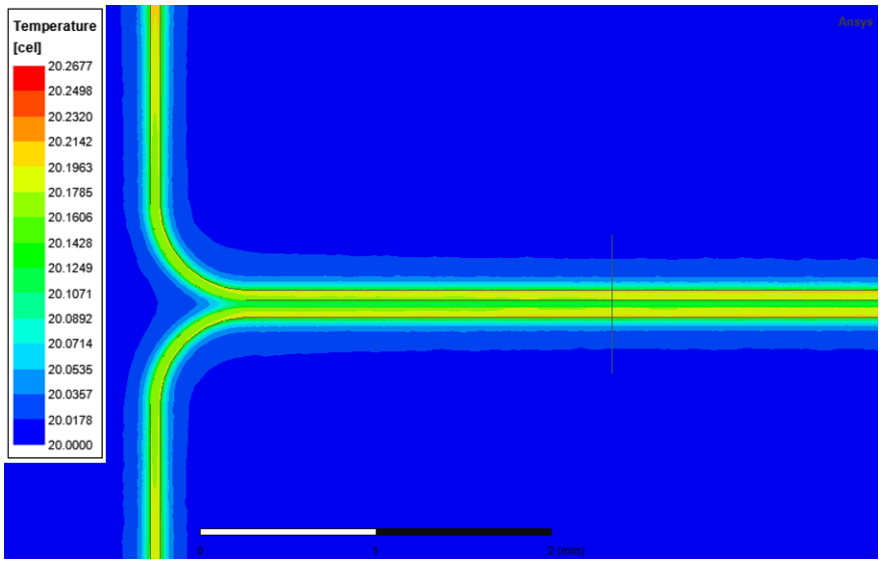

Figure 3: Thermal simulation of atom chip with thick ground plane, phase difference $\phi = 0°$, and 20 W/mK AlN bulk conductivity, showing peak temperature of approximately 20.27°C.

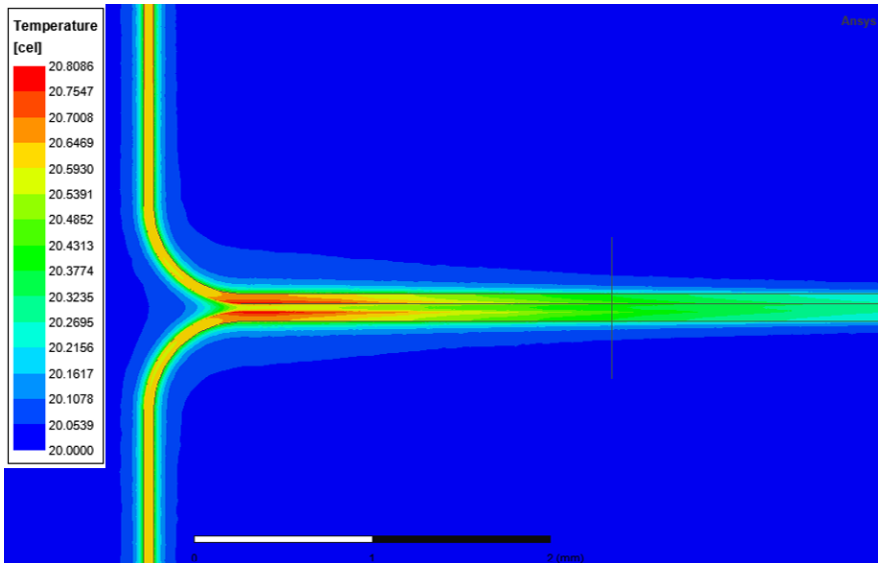

Figure 4: Thermal simulation of atom chip with thick ground plane, phase difference $\phi = 180°$ and 20 W/mK AlN bulk conductivity, showing peak temperature of approximately 20.8°C.

In the case of the thick ground plane, the temperature only rose from 20.27°C to 20.8°C with a change in phase difference from $\phi = 0°$ to $\phi = 180°$. The thick ground plane model yields a ΔT=0.53°C between even and odd mode operation, compared to ΔT=4.40°C for the thin ground plane model. From these results, it was determined that using the 1 mm thick copper ground plane was ideal.